# AN IMPLICIT SOLUTION OF THE THREE-DIMENSIONAL NAVIER-STOKES EQUATIONS FOR AN AIRFOIL SPANNING A WIND TUNNEL

By

ANUTOSH MOITRA

A Dissertation
Submitted to the Faculty of
Mississippi State University
in Partial Fulfillment of the Requirements
for the Degree of Doctor of Philosophy
in the College of Engineering

Mississippi State, Mississippi

August 1982

For

My Parents

## ACKNOWLEDGEMENTS

This dissertation would not have been possible without the superb counsel and perspicacity of my advisor, Dr. Joe F. Thompson. Listed below are some of the others who made noteworthy contributions to this long and sometimes dreary, but ultimately rewarding endeavor.

| | |
|---|---|
| Bob Bernard, Mike Freeman and Johnny P. Ziebarth | Excellent friends and co-sufferers. |
| Rita Curry | Outstanding typist and caring editor. |
| Dr. A. G. Bennett | Instigator. |

Then there is that host of others who, in their own individual ways, helped dispel some of the drudgery, and made the ordeal survivable while demanding no conspicuousness. The tribute to this nameless horde is best left tacit. The omission of acknowledgements by names, therefore, resulted from the fondest intentions and not from neglect.

This research was sponsored by NASA Grant NSG 1623, Langley Research Center.

Thank you.

A. M.

Mississippi State University

August 1982

## ABSTRACT

Anutosh Moitra, Doctor of Philosophy, 1982

Major: Engineering, Department of Aerospace Engineering

Title of Dissertation: An Implicit Solution of the Three-Dimensional Navier-Stokes Equations for an Airfoil Spanning a Wind Tunnel

Directed by: Dr. Joe F. Thompson

Pages in Dissertation: 78 Words in Abstract: 280

### Abstract

An implicit finite-difference algorithm is developed for the numerical solution of the incompressible three-dimensional Navier-Stokes equations in the non-conservative primitive-variable formulation. The algorithm is second-order-space-time accurate, iterative and employs a point SOR method for solution.

The flow field about an airfoil spanning a wind-tunnel is computed. The coordinate system is generated by an extension of the two-dimensional body-fitted coordinate generation techniques of Thompson, as well as that of Sorenson, into three dimensions. Two-dimensional grids are stacked along a spanwise coordinate defined by a simple analytical function.

A Poisson pressure equation for advancing the pressure in time is arrived at by performing a divergence operation on the momentum equations. The pressure at each time-step is calculated on the assumption that continuity be unconditionally satisfied. An eddy viscosity coefficient, computed according to the algebraic turbulence formulation of Baldwin and Lomax, simulates the effects of turbulence.

Computational Results are presented for the NACA 0012 and NACA $66_3018$ airfoils in simulated wind-tunnel tests. Computations were performed for a Reynolds number of 1000 for the NACA 0012 airfoil at angles of incidence of 0 and 12 degrees. They Reynolds number was increased to 10,000 for computations with the NACA $66_3018$ airfoil as the profile under investigation. Pressure plots and velocity profiles are presented for the various cases. Comparison with wind-tunnel data for the NACA $66_3018$ airfoil indicates qualitative agreement with typical pressure distributions. Quantitative replication of experimental data was beyond the scope of this dissertation, what with scant data points in the discrete mesh system and the consequent inability to perform computations at high Reynolds numbers. The size of the grids and the total computation time were restricted by considerations of affordability. The feasibility of an implicit solution of the complete three-dimensional Navier-Stokes equations is established and sufficient encouragement for future computations at realistically high Reynolds numbers is derived.

TABLE OF CONTENTS

## NOMENCLATURE

**Symbols**

| | |
|---|---|
| A | Angle of Attack |
| $C_p$ | Pressure Coefficient |
| D | Divergence of Velocity Vector |
| $\underset{\sim}{i}, \underset{\sim}{j}, \underset{\sim}{k}$ | Cartesian Unit Vectors |
| IMAX, JMAX, KMAX | Number of $\xi$, $\eta$, and $\zeta$-lines in Transformed Plane |
| J | Jacobian of Coordinate Transformation, Eq. (A.4 ) and (A.13) |
| $\underset{\sim}{n}$ | Unit Normal Vector |
| P | Pressure |
| $R_e$ | Reynolds Number |
| t | Time |
| $\underset{\sim}{u}$ | Velocity Vector |
| u | x - Component of Velocity |
| v | y - Component of Velocity |
| w | z - Component of Velocity |
| x, y, z | Cartesian Coordinates |
| $\xi$, $\eta$, $\zeta$ | Curvilinear Coordinates |
| $\alpha$, $\beta$, $\gamma$, $\delta$, $\sigma$, $\tau$, $\phi$ | Coordinate Transformation Parameters, Appendix A. |
| $\varepsilon$ | Eddy Viscosity |
| $\theta$ | Artificial Viscosity |
| $\omega$ | Acceleration Parameter for SOR |
| $\underset{\sim}{\nabla}$ | Del-operator, $\underset{\sim}{\nabla} \equiv \underset{\sim}{i} \frac{\partial}{\partial x} + \underset{\sim}{j} \frac{\partial}{\partial y} + \underset{\sim}{k} \frac{\partial}{\partial z}$ |

**Superscripts**

| | |
|---|---|
| n | Time-step Index |
| (s) | Iteration Count |
| (ξ) | Pertains to Constant ξ-Surface |
| (η) | Pertains to Constant η-Surface |
| ' | Denotes First Derivative |
| '' | Denotes Second Derivative |
| • | Degree (Angle) |

**Subscripts**

| | |
|---|---|
| i, j, k | Designates Position in Mesh System |
| ITU, ITL | Denotes Trailing Edge i-index value on Upper and Lower Surfaces of Airfoil |
| min, max | Denotes Minimum and Maximum Value |
| t, x, y, z, ξ, η, ζ | Denotes First Partial Differentiation |
| xx, yy, zz, ξξ, ηη, ζζ | Denotes Second Partial Differentiation |
| ξη, ηζ, ξζ | Denotes Cross Partial Differentiation |
| ∞ | Denotes Infinity Condition |

## LIST OF FIGURES

# Chapter I

## Introduction and Literature Review.

The importance of and the necessity for computer solutions of the complete three-dimensional Navier-Stokes equations as a reliable alternative to experimental fluid-dynamic studies cannot be over emphasized. It was, therefore, not the lack of intellectual motivation and initiative but rather that of sufficient advances in computer technology that limited the researchers' involvement in this field since the beginning of the computational fluid dynamic era in the early 1960's. Graves [1] has given a comprehensive overview of the evolution of the CFD discipline. Until the advent of the supercomputers the CPU time as well as storage requirements associated with three-dimensional Navier - Stokes solutions were truly prohibitive. These difficulties have been partially overcome by recent computers with radically changed architectures permitting enormously increased speed and storage capacity, particularly the CDC 200 series and the CRAY 1 machines.

The two chief tasks comprising fluid dynamic computations, namely effective grid generation and developing accurate algorithms for solving the governing equations play complementary roles to each other. Consequently, advances in the techniques in these two fields have gone hand in hand. The concept of boundary-fitted coordinate systems developed by Thompson, et. al. [2], has established itself as particularly suitable for effective grid generation for arbitrary shaped bodies. Sorenson , et. al. [3], offer a different version of the body-fitted grid generation technique. Both these techniques are extensible into three dimensions for bodies with simple geometries without necessitating

any rigorous mathematics. Boundary-fitted coordinate systems permit computation in a rectangular grid with straight boundaries in the transformed plane, thus making the implementation of boundary conditions much simpler than in the physical plane with arbitrarily shaped boundaries.

A primitive variable formulation of the complete Navier-Stokes equations is advantageous for three-dimensional flow computations. Various methods, each with its own area of applicability, have been formulated and successfully executed by researchers in flow situations of different characteristics. These methods can be broadly categorized into explicit and implicit algorithms; their relative advantages being less computer storage requirements and greater speed respectively.

Explicit techniques are restricted by time-step size limitations dictated by stability considerations. Among implicit techniques the Approximate Factorization technique, formulated by Beam and Warming [4], has been successfully used in computation of compressible flow, but is not readily applicable to incompressible flow. However, modified versions of AF techniques have been used by Steger and Kutler [5] and Bernard [6] for attempting incompressible flow computations. Given the above considerations and the task of solving the complete three-dimensional Navier-Stokes equations, a fully implicit scheme employing successive over-relaxation (SOR) emerged as the logical alternative. Available information on numerical solution of three-dimensional incompressible turbulent flow is scarce. East and Pierce [7], provide one of the very few publications in this field.

The three-dimensional coordinate systems for the problem at hand

are generated by means of extensions of the 2-D boundary-fitted grid generation techniques of Thompson [8] and Sorenson [3]. The spanwise extent of the coordinate system is achieved by stacking a number of 2-D C-type grids along the span of the wing. Coordinate lines are made to concentrate in the boundary layers on body surfaces, i.e., the wind tunnel walls as well as the airfoil. Computations for the velocities and the pressure are performed in the transformed plane.

The governing equations are the incompressible Navier-Stokes equations written in their non-conservative forms in terms of the primitive variables. A Poisson equation for pressure is obtained by taking the divergence of the momentum equations. The eddy viscosity in the Reynolds-averaged momentum equations is derived from a two-layer algebraic turbulence model as proposed by Baldwin and Lomax [9]. Boundary conditions imposed on the walls of the wind tunnel and the airfoil are obtained employing no-slip conditions for velocities and the normal derivative of pressure from the momentum equations evaluated on the boundaries. Constant free-stream conditions are imposed on the upstream boundary. The flow is initiated by using a cosine body force to gradually accelerate the airfoil together with its attached coordinate system from rest to the free-stream velocity over a period of time.

A fully implicit algorithm is obtained by representing the non-dimensional Navier-Stokes equations by second-order backward-time and central-space finite difference approximations in the transformed coordinate plane. The resulting coupled system of nonlinear algebraic equations is solved by means of a point successive over-relaxation (SOR) iterative method with locally optimum acceleration parameters

The development of the algorithm was along the lines followed by Thomspon [13] in two-dimensional computations.

The succeeding chapters of this dissertation deal in further detail with the coordinate generation techniques, the formulation of the governing equations and the implementation of the numerical techniques in that order. It was the desire of the author to present the essence of the elements involved without burdening the reader with cumbersome repetitions. Solving the complete three-dimensional Navier-Stokes equations should be tantamount to generating and analyzing all the flow phenomena arising out of a given fluid-body configuration. It is the hope of progress towards achieving this cherished goal of researchers in computational fluid dynamics that motivated this research.

## Chapter II

## The Coordinate System.

### 2.1 The boundary-fitted concept.

A proper coordinate system can be a quite unforgiving prerequisite for the ease and accuracy of solution of a physical problem. The propriety consists mainly of freedom as to the shape of the body being investigated. Realistic aerodynamic problems rarely involve body surfaces amenable to analytical representation and often include sharp corners implying discontinuous slopes. A Cartesian coordinate system under such circumstances would be limited in efficacy by the need for interpolation near the boundary surfaces.

The boundary-fitted coordinate system of Thompson, et. al. [8], provides a set of curvilinear coordinates with one line of each family coincident with a boundary in the physical domain. This eliminates the need for interpolation and results in a complete freedom regarding the shape of the bodies involved. It has the added capability for concentrating coordinate lines in regions where large gradients in the physical quantities are expected to arise.

### 2.2 Theoretical Formulation

Computational grid generation in its essence consists of a mapping between real and computational spaces. The physical space defined by Cartesian coordinates x and y is mapped onto the computational space through the mapping functions

$$\xi = \xi (x, y) \tag{2.1}$$

and $$\eta = \eta (x, y)$$

One-to-one correspondence is ensured by subjecting $\xi$ and $\eta$ to the sufficient, though not necessary, conditions of satisfying the extremum principle and of monotonic variation in $\xi_{min} \leq \xi \leq \xi_{max}$ and $\eta_{min} \leq \eta \leq \eta_{max}$. The extremum principle precludes occurrence of extrema in $\xi$ and $\eta$ within the field and is complied with by making the inner and the outer boundaries coincide with the $\eta = \eta_{min}$ and the $\eta = \eta_{max}$ lines respectively, while $\xi_{min}$ and $\xi_{max}$ occur on the cutflow boundary.

The topological correspondence in a C-type grid about a 2-D airfoil may be better understood with the help of Figure 1. The boundary $\eta = \eta_{max}$ is mapped onto the inner boundary $\Gamma_5 - \Gamma_1 - \Gamma_6$ containing the branch cuts and the airfoil. $\xi = \xi_{min}$ and $\xi = \xi_{max}$ correspond to the downstream sections $\Gamma_{7L}$ and $\Gamma_{7U}$ respectively, $\xi$ increasing clockwise around the airfoil. The $\eta$ = constant family of lines form open curves resembling the letter C. The $\eta = \eta_{max}$ boundary is mapped onto the outer boundary $\Gamma_2 - \Gamma_4 - \Gamma_3$ comprised of the wind tunnel walls and the inflow section $\Gamma_4$.

With the afore-mentioned desired characteristics of $\xi$ and $\eta$ in mind, it is natural to envision them as solutions of elliptic partial differential equations with Dirichlet boundary conditions. Elliptic equations permit any desired distribution of $\xi$ and $\eta$ on the boundaries. Moreover, the inherent smoothness of solutions of elliptic systems is well recognized. The choice of elliptic systems is further reinforced by the ability of the inhomogenous terms in Poisson's equations to control coordinate line spacing with respect to curve or a point within the field. The generating system of Poisson's equations has the following form:

$$\xi_{xx} + \xi_{yy} = \frac{\alpha_c}{J_c^2} P(\xi,\eta)$$

$$\eta_{xx} + \eta_{yy} = \frac{\gamma_c}{J_c^2} Q(\xi,\eta) \qquad (2.2)$$

A judicious choice of the distributions of P and Q makes it possible to concentrate lines in any desired region. Section 2.3 deals with actual forms of P and Q in further detail. An interchange of dependent and independent variables enables one to perform all computations in the transformed field. The generating system in the transformed field becomes:

$$\alpha_c x_{\xi\xi} - 2\psi_c x_{\xi\eta} + \gamma_c x_{\eta\eta} = -(\alpha_c x_\xi P(\xi,\eta) + \gamma_c x_\eta Q(\xi,\eta) )$$

$$\alpha_c y_{\xi\xi} - 2\psi_c y_{\xi\eta} + \gamma_c y_{\eta\eta} = -(\alpha_c y_\xi P(\xi,\eta) + \gamma_c y_\eta Q(\xi,\eta) ) \qquad (2.3)$$

the boundary conditions being specified for x and y by the known shape of the body surfaces. The coefficients in the system 2.3 have forms given below:

$$\alpha_c = x_\eta^2 + y_\eta^2 \qquad (2.4)$$

$$\psi_c = x_\xi x_\eta + y_\xi y_\eta \qquad (2.5)$$

$$\gamma_c = x_\xi^2 + y_\xi^2 \qquad (2.6)$$

$$J_c = x_\xi y_\eta - x_\xi y_\eta \qquad (2.7)$$

The increased complexity of the transformed equations (2.3) compared with equations (2.2) is far overshadowed by the ease of implementing boundary conditions on straight boundaries in the transformed plane.

A great deal of simplification in computation results if integer values are assigned to $\xi$ and $\eta$. To this end, increments $\Delta\xi$ and $\Delta\eta$ are

chosen to be unity by construction. This gives rise to uniform spacing in the transformed plane where the values of $\Delta\xi$ and $\Delta\eta$ , rather than those of $\xi$ and $\eta$ are relevant to the finite difference expressions. The generating system of equations (2.3) is represented by second-order finite difference approximations in the transformed plane. The quantities $\Delta\xi$ and $\Delta\eta$ disappear by cancellation in all difference equations. The resulting system of non-linear difference equations is solved by means of a point SOR iterative scheme.

## 2.3 Coordinate Line Concentration

It is imperative to concentrate coordinate lines in regions with large gradients in flow variables, e.g., near body surfaces. Thompson et. al. [10], and Sorenson achieve this effect in two different ways.

### 2.3.1 Thompson et. al. approach

Thompson's approach consists of finding a correspondence between $\eta$ values and the radii of concentric circles distributed between two circles with radii $r_1$ and $r_2$, one circumscribing the airfoil and the other tangential to the outer boundary respectively. Applying the coordinate generating equations (2.3) to the radii $r_1$ and $r_2$, while noting that $\eta = 1$ on the airfoil and $\eta = J$ on the outer boundary, results in the following expression for Q:

$$Q(\xi,\eta) = -\left(\frac{r''}{r} - \frac{r'}{r}\right) \tag{2.8}$$

where

$$r(\eta) = r_2 + \frac{G(\eta) - 1}{G(\eta) + 1}\left(1 - \frac{r_1}{r_2}\right)b \tag{2.9}$$

and

$$G(\eta) = \left(\frac{b + r_2}{b - r_2}\right)^{\left(\frac{\eta - J}{J - 1}\right)} \tag{2.10}$$

The effect of Q, thus defined, is to place a line corresponding to $\eta = K$ at a distance proportional to $r_K - r_1$ from the body surface. In order to ensure proper resolution of the boundary layer the first line away from the boundary is placed at an approximate distance of one percent of the Blasius flat-plate boundary layer thickness from the body, i.e.,

$$r_{(\eta = 2)} - r_1 = 0.01\left(\frac{5}{\sqrt{R_e}}\right) \tag{2.11}$$

2.3.2 Sorenson's Approach

Sorenson [3] determines the control functions P and Q iteratively to produce specified spacing S of the first $\eta$-line from the boundary and a specified angle of intersection $\theta$ of $\xi$-lines with the boundary (fig. 2).

P and Q are defined as:

$$P(\xi, \eta) = p(\xi)e^{-a\eta} + r(\xi)e^{-c(\eta_{max} - \eta)} \tag{2.11a}$$

$$Q(\xi, \eta) = q(\xi)e^{-b\eta} + s(\xi)e^{-d(\eta_{max} - \eta)} \tag{2.11b}$$

where a, b, c and d are positive constants. The coefficients of r and s become vanishingly small at the body ($\eta = 0$), so that

$$P(\xi, 0) = p(\xi)$$

$$Q(\xi, 0) = q(\xi) \tag{2.12}$$

Similarly at the outer boundary ($\eta = \eta_{max}$) ,

$$P(\xi, \eta_{max}) = r(\xi)$$

$$Q(\xi, \eta_{max}) = s(\xi) \tag{2.13}$$

Combining equations 2.12 with the generating system of equations 2.3 we get

$$p(\xi) = \left[\frac{Y_\eta R_1 - X_\eta R_2}{J_c}\right]_{\eta = 1} \qquad q(\xi) = \left[\frac{-Y_\xi R_1 + X_\xi R_2}{J_c}\right]_{\eta = 1} \quad (2.14)$$

where,

$$R_1 = \left[\frac{-(\alpha X_{\xi\xi} - 2\beta X_{\xi\eta} + \alpha X_{\eta\eta})}{J_c^2}\right]_{\eta = 1} \qquad R_2 = \left[\frac{-(\alpha Y_{\xi\xi} - 2\beta Y_{\xi\eta} + Y_{\eta\eta})}{J_c^2}\right]_{\eta = 1} \quad (2.15)$$

Similar expressions for $r(\xi)$ and $s(\xi)$ are obtained from equations 2.13 and 2.3.

The steps involved in the iterative method for generating the grid can be summarized as follows:

1. The four geometric constraints of specified spacing and angle of intersection at the inner and outer boundaries translate into equations which can be solved for all the derivatives occurring in equations 2.14 except $X_{\eta\eta}$ and $Y_{\eta\eta}$ on the boundaries.

2. Assumed initial values of p, q, r and s are used to determine P and Q in the field.

3. The elliptic generating system, (2.3), is solved for X and Y in the field.

4. $X_{\eta\eta}$ and $Y_{\eta\eta}$ are computed on the boundaries.

5. p, q, r, s and subsequently P and Q are determined from equations 2.14 and 2.15.

Steps 3 to 5 are iterated to convergence.

## 2.4 The 3-D extension.

So far the generation of 2-D grids has been discussed. The body under investigation is a 2-D wing spanning a wind tunnel and therefore, an extension of the 2-D grid into three dimensions is necessary. This has been achieved in a straight forward way by placing 2-D grids at different stations along the span as illustrated in figure 3. Since no change in airfoil geometry occurs along the span, it is sufficient to perform flow calculations on only one side of the mid-span section. An extra grid has been placed beyond the mid-span section for storing variables in order to facilitate finite differencing.

The 2-D grids are identical to each other so that X and Y are independent of Z, the Cartesian coordinate along the span. Consequently, Z is a simple analytical function of $\zeta$,

$$Z = F(\zeta)$$

$\zeta$, being the third mapping function introduced by the 3-D extension.

F can be chosen to be an exponential function in order to effect a desired distribution of the grids along the span.

## Chapter III

## The Governing Equations

### 3.1 The Navier-Stokes equations

The Navier-Stokes equations, derived from Newton's law of conservation of momentum and Stokes' law regarding relationships between stress and strain in a material fluid volume, remain to date the most versatile descriptor of fluid motion. The governing equations in this study are the time-dependent, incompressible, Reynolds averaged Navier-Stokes equations in three dimensions formulated in terms of the primitive variables.

In their unabridged form the Navier-Stokes equations are as they appear below:

$$\frac{\partial(\rho u_i)}{\partial t} + \frac{\partial(\rho u_i u_j)}{\partial x_j} = -\frac{\partial P}{\partial x_i} + \frac{\partial \Sigma_{ij}}{\partial x_j} + \rho g_i \qquad (3.1)$$

$$\frac{\partial \rho}{\partial t} + \frac{\partial(\rho u_j)}{\partial x_j} = 0 \qquad (3.2)$$

The index i denotes the Cartesian directions $x_1$, $x_2$ and $x_3$; and j is subject to the Einstein summation convention. The quantities represented in these equations are

$\rho$ = density

$u_i$ = velocity component

$P$ = Pressure

$\Sigma_{ij}$ = shear stress tensor = $\mu\left(\frac{\partial u_i}{\partial x_j} + \frac{\partial u_j}{\partial x_i}\right) - \frac{2}{3}\mu \frac{\partial u_k}{\partial x_k} \delta_{ij}$

$g_i$ = body force per unit mass

(3.1) represents the momentum equations governing fluid flow while (3.2) is the equation of continuity. These equations are direct differential descendants of their integral forms in terms of conserved quantities. In this "conservative" form the equations are particularly effective in flow regions containing discontinuities. Since the flow under investigation in this research contains no such discontinuities, a further simplification can be effected by incorporating the continuity equation (3.2) into the momentum equation (3.1) in the following manner.

Expansion of all the derivatives in equation (3.1) and rearrangement of the quantities while noting that the density $\rho$ is a constant in incompressible flow reduce the equations to

$$\frac{\partial u_i}{\partial t} + u_j \frac{\partial u_i}{\partial x_j} + u_i \frac{\partial u_j}{\partial x_j} = -\frac{1}{\rho}\frac{\partial P}{\partial x_i} + \frac{1}{\rho}[\mu \nabla^2 u_i + \mu \frac{\partial}{\partial x_i}(\frac{\partial u_j}{\partial x_j}) + \frac{\partial \mu}{\partial x_j}(\frac{\partial u_i}{\partial x_j} + \frac{\partial u_j}{\partial x_i})] + g_i \qquad (3.3)$$

and,

$$\frac{\partial u_j}{\partial x_j} = 0 \qquad (3.4)$$

The third terms on both sides of the sign of equality in equation (3.3) vanish by virtue of equation (3.4), implying that continuity is assumed to be unconditionally preserved in the flow. The products of this manipulation are the following "non-conservative" governing equations:

$$\frac{\partial u_i}{\partial t} + u_j \frac{\partial u_i}{\partial x_j} = -\frac{1}{\rho}\frac{\partial P}{\partial x_i} + \frac{1}{\rho}[\mu \nabla^2 u_i + \frac{\partial \mu}{\partial x_j}(\frac{\partial u_i}{\partial x_j} + \frac{\partial u_j}{\partial x_i})] + g_i \qquad (3.5)$$

$$\frac{\partial u_j}{\partial x_j} = 0 \qquad (3.6)$$

Additional cogency is lent to the arguments for choosing the non-conservative form of the governing equations by the fact that nullity of the divergence of velocities, i.e., continuity, is a requirement essential to the scheme for advancing the pressure in time as will be demonstrated in a latter section in this chapter.

Finally, the governing equations are rid of dimensions by substituting the flow variables with the following non-dimensional quantities:

$$\ddot{u}_i = u_i/U_\infty \tag{3.7}$$

$$\ddot{x}_i = x_i/\ell \tag{3.8}$$

$$\ddot{t} = tU_\infty/\ell \tag{3.9}$$

$$\ddot{\mu} = \mu/\mu_\infty \tag{3.10}$$

$$\ddot{P} = (P - P_\infty)/(\rho U_\infty^2) \tag{3.11}$$

$$\ddot{g}_i = g_i \ell/U_\infty^2 \tag{3.12}$$

where the characteristic quantities are the free-stream velocity $U_\infty$, the airfoil chord length $\ell$, and the free-stream viscosity $U_\infty$.

The resulting non-dimensionalized Navier-Stokes equations governing incompressible flow are:

$$\frac{\partial \ddot{u}_i}{\partial \ddot{t}} + \ddot{u}_j \frac{\partial \ddot{u}_i}{\partial \ddot{x}_j} = -\frac{\partial \ddot{P}}{\partial \ddot{x}_i} + \frac{1}{R_e}[\ddot{\mu}\nabla^2 \ddot{u}_i + \frac{\partial \ddot{\mu}}{\partial \ddot{x}_j}(\frac{\partial \ddot{u}_i}{\partial \ddot{x}_j} + \frac{\partial \ddot{u}_j}{\partial \ddot{x}_i})] + g_i \tag{3.13}$$

and

$$\frac{\partial \ddot{u}_i}{\partial \ddot{x}_j} = 0 \tag{3.14}$$

$$R_e = \frac{\rho U_\infty \ell}{\mu_\infty}$$ $R_e$ denotes the Reynolds number.

The remainder of this dissertation deals exclusively with non-dimensional quantities and therefore the diereses (") will not appear henceforth.

In usual Cartesian notation the governing equations (3.13) and (3.14) translate to,

$$u_t + uu_x + vu_y + wu_z = - P_x + \frac{1}{R_e}[\mu\nabla^2 u + 2\mu_x u_x + \mu_y(u_y + v_x) + \mu_z(w_x + u_z)] + g_1 \qquad (3.15)$$

$$v_t + uv_x + vv_y + wv_z = - P_y + \frac{1}{R_e}[\mu\nabla^2 v + 2\mu_y v_y + \mu_z(v_z + w_y) + \mu_x(u_y + v_x)] + g_2 \qquad (3.16)$$

$$w_t + uw_x + vw_y + ww_z = - P_z + \frac{1}{R_e}[\mu\nabla^2 w + 2\mu_z w_z + \mu_x(w_x + u_z) + \mu_y(w_y + v_z)] + g_3 \qquad (3.17)$$

and,

$$u_x + v_y + w_z = 0 \qquad (3.18)$$

3.2 Turbulence modelling.

The effects of turbulence are simulated by appending an eddy viscosity coefficient $\mu_T$ to the molecular coefficient of viscosity $\mu$. The scheme for determining $\mu_T$ is patterned after that of Baldwin and Lomax [9], who devised a two-layer algebraic turbulence model for separated flows. The non-dimensional viscosity coefficient in equations (3.15) - (3.17) is replaced by

$$\mu = 1 + \epsilon \qquad (3.18)$$

where $\epsilon$ is the ratio of $\mu_T$ to the molecular coefficient of viscosity. A few salient features of the turbulence model are:

1)The need for finding the edge of the boundary layer is obviated by using the distribution of vorticity to determine length scales.

2)An intermittency factor is employed in order to modify the eddy viscosity coefficient in transitional regions.

3)Transition is assumed to occur at the points of minimum pressure on the upper and the lower surfaces of the airfoil.

## 3.3 The pressure equation.

A direct temporal discretization of pressure is not possible because of the absence of a time-derivative of pressure in the governing equations (3.15) - (3.17). Advancement of pressure in time, unlike that of the velocities, is therefore not a straightforward task. The difficulty can, however, be circumvented by a stratagem of determining the instantaneous pressure subject to the constraint of satisfying continuity throughout the flow field. In other words, the pressure adjusts itself in order to force the divergence of the velocity vector to zero, implying a strict conservation of mass.

To achieve this purpose a divergence operation is performed on the momentum equations (3.15) - (3.17) to arrive at the following Poisson equation for pressure.

$$D_t + \nabla^2 P = -(u_x^2 + v_y^2 + w_z^2 + 2v_x u_y + 2\, w_x u_z + 2w_y v_z) + \frac{2}{R_c}[\mu_x \nabla^2 u + \mu_y \nabla^2 v + \mu_z \nabla^2 w + \mu_{xx} u_x + \mu_{yy} v_y + \mu_{zz} w_z + \mu_{xy}(u_y + v_x) + \mu_{zx}(w_x + u_z) + \mu_{zy}(v_z + w_y)] \qquad (3.19)$$

where D is the divergence, $u_x + v_y + w_z$, of the velocity vector.

Several variations on this theme have been presented by Hodge [11] and Shanks [12]. In the non-conservative equation (3.18) $D_t$ is expected to retain an appreciable value even though D is assumed to be analytically zero. From a computational point of view $D_t$ serves as a corrective term that adjusts the pressure in an effort to enforce the continuity constraint.

## 3.4 Coordinate transformation.

The governing equations must be transposed to the computational grid before performing the finite difference approximations on the derivatives. The spatial derivatives must be transformed by the inclusion of terms, relating the discrete mesh to the physical grid, in order to remove the physical coordinate system from the problem.

The derivatives, $u_x$, $u_{xx}$, etc. in equations (3.15) - (3.17) are therefore substituted by their values computed according to the expressions for the derivatives in the transformed plane listed in appendix A.

## Chapter IV

### The Boundary Conditions.

The solution of the Navier-Stokes equations is a quintessential boundary value problem. Extreme care must be exercised in specifing the boundary conditions, since the validity of the solution is dependent on the accuracy of the boundary values. Presented below are the velocity and pressure conditions applied on the various boundaries occurring in the flow.

### 4.1 Free-stream boundary conditions and initial values.

The inflow section $\Gamma_4$ in Figure 1, is identified with a free-stream boundary on the assumption that it is far enough removed from the bodies in the flow so that the incident uniform flow conditions here are unperturbed by the presence of the bodies. Since the free-stream in this study is considered to be a uniform parallel flow, constant values for velocities and the pressure are always specified on this boundary.

However, the presence of the accelerating body force $g_i$ in equations (3.15) - (3.17) imply that the incident velocities change with time; starting from a zero value until they reach their ultimate prescribed non-dimensional values. The boundary conditions on $\Gamma_4$ are therefore,

$$
\begin{aligned}
u_\infty &= \int_0^t g_1 \, dt, \text{ so that } (0 \leq u_\infty \leq 1) \in (0 \leq t \leq 1) \\
v_\infty &= 0 \; ; \; g_2 = 0 \\
w_\infty &= 0 \; ; \; g_3 = 0 \\
P_\infty &= 0
\end{aligned}
\qquad (4.1)
$$

On the outflow boundaries ($\Gamma_{7u}$, $\Gamma_{71}$), the gradients of the flow variables are specified. Denoting the normal to the outflow boundary by $\underset{\sim}{n}$, the outflow conditions can be written as

$$\underset{\sim}{n} \cdot \underset{\sim}{\nabla} u = 0$$

$$\underset{\sim}{\nabla} P = 0 \qquad (4.2)$$

4.2 Boundary conditions on body surfaces.

The flow region is bounded by a number of body surfaces of different families, consisting of the containing walls of the wind tunnel and the wing spanning it. The airfoil and the top and the bottom walls of the wind tunnel, sections $\Gamma_1$, $\Gamma_2$ and $\Gamma_3$ coincide with $\eta$ = constant surfaces. The end wall, k = 1 in figure 3, represents the $\zeta = 1$ surface. The wall corresponding to $\zeta = \zeta_{max}$ need not be considered because the flow is assumed to be symmetrical about the centre-span section at k = 4. In the absence of transpiration at these material surfaces the velocity boundary conditions belong to the genre known as no-slip boundary conditions for viscous flow. A complete absence of relative motion, 'slip', between the solid surfaces and the adjoining fluid layers is assumed and the velocity boundary conditions are defined by

$$u = 0$$

$$v = 0 \qquad (4.3)$$

$$w = 0$$

Boundary values for pressure on body surfaces are calculated by designing a momentum equation that is satisfied by the component of the pressure gradient normal to the body surface. An expression for the normal pressure gradient, which leads to a Neumann type

boundary condition, is obtained making use of the relations for the directional derivative $\underset{\sim}{n}$ normal to a surface of constant $\eta$ and constant $\zeta$ (Appendix A) as,

$$\underset{\sim}{n} \cdot \nabla P = \underset{\sim}{n} \cdot (\underset{\sim}{g} + \frac{1}{R_e} \nabla^2 \underset{\sim}{u}) \tag{4.4}$$

A further simplification results from neglecting the viscous terms in the boundary layer and equation (4.4) reduces to

$$\underset{\sim}{n} \cdot \nabla P \simeq \underset{\sim}{n} \cdot \underset{\sim}{g} \tag{4.5}$$

The top and the bottom walls of the wind tunnel ($\Gamma_2$ and $\Gamma_3$), are coincident with parts of the $\eta = \eta_{max}$ boundary, while the airfoil ($\Gamma_1$) forms a part of the $\eta = \eta_1$ surface. These boundaries are therefore referred to as $\eta$-surfaces. The component of the momentum equation normal to a constant $\eta$-surface, obtained by replacing $\underset{\sim}{n}$ by $\underset{\sim}{n}^{(\eta)}$ in equation (4.5) is,

$$-P_x Y_\xi + P_y X_\xi = - Y_\xi g_1 + X_\xi g_2 \tag{4.6}$$

The expression for $\underset{\sim}{n}^{(\eta)}$, the normal to constant $\eta$-surfaces, is given in Appendix A. Using the coordinate transformations for $P_x$ and $P_y$ and rearranging the terms in equation (4.6) the $\eta$-derivative of pressure on the boundary is obtained as,

$$P_\eta = \frac{1}{\alpha_c} [P_\xi \beta_c + J_c(- y_\xi g_1 + x_\xi g_2)] \tag{4.7}$$

The surface pressure is evaluated from a one sided finite difference approximation for $P_\eta$.

An expression similar to equation (4.7) is obtained for $\zeta$-surfaces employing $\underset{\sim}{n}^{(\zeta)}$, the normal to a $\zeta$-surface, in equation (4.5). The resulting Neumann pressure boundary condition for the k = 1 wall (figure 3), is given by

$$\frac{P_\zeta}{F'(\zeta)} = g_3 \tag{4.8}$$

where,

$F'(\zeta)$ is defined as,

$$F'(\zeta) = Z_\zeta \tag{4.9}$$

The Dirichlet velocity boundary conditions (4.5) together with the Neumann pressure boundary conditons (4.7) or (4.8) describe the boundary values on all material surfaces.

## 4.3 Conditions on the re-entrant sections.

The re-entrant sections, $\Gamma_5$ and $\Gamma_6$ in figure 1, are not boundaries in the physical plane but represent points within the flow field. These sections originate from the branch cut from the trailing edge of the airfoil to the outflow boundary, made in a C-type grid in order to eliminate discontinuity in the geometry of the inner boundary. Application of boundary conditions, in the strictest sense, on these sections is therefore redundant and not allowed. Maintaining continuity in the flow variables and their gradients across the cut is de rigueur. Values of velocity and pressure on these sections should therefore emerge as a part of the field solution. However, since the re-entrant sections form parts of the $\eta = 1$ boundary in the computational plane, they may be considered subject to a periodic set of boundary conditions.

## 4.4 Conditions at the trailing edge.

The trailing edge is often a sharp point in the physical plane. Though the inner boundary, $\eta = 1$, is a continuous line in the computational plane, the surface-normal vector to the $\eta$-surface, $n^{(\eta)}$ is

still discontinuous at the trailing edge. The surface pressures at the top and the bottom trailing edge points, computed according to equation (4.7) are therefore apt to disagree with each other. The unequal trailing edge pressures would violate the assumption of absence of any unbalenced forces as implied in the no-slip conditions.

It was deemed advantageous to determine the pressure at the trailing edge point by means of an average of extrapolates. The extrapolates $P_{TL}$ and $P_{TU}$ were calculated from expressions arrived at by representing $P_{\xi}$ with a three-point one-sided finite difference approximation. The extrapolates are given by,

$$P_{ITL} = \frac{1}{3}(4P_{ITL + 1} - P_{ITL + 2}) \tag{4.10}$$

and

$$P_{ITU} = \frac{1}{3}(4P_{ITU-1} - P_{ITU - 2}) \tag{4.11}$$

ITL and ITU denote the indices in the $\xi$-direction corresponding to the lower and the upper trailing edge points respectively.

## 4.5 Plane of symmetry conditions.

As mentioned earlier, computations are performed only on one side of the plane of symmetry situated at the mid-span section of the wing. In the computational context the second boundary in the z-direction needs to be a grid placed beyond the mid-span section so that values of the flow variables can be carried over from the grid stationed immediately before the mid-span in order to ensure symmetry of the flow. Denoting the k-index of the centre-span grid by kc, the following substitutions are made prior to each SOR iteration.

$$u_{kc + 1} = u_{kc - 1} \tag{4.12}$$

$$v_{kc+1} = v_{kc-1} \tag{4.13}$$

$$w_{kc+1} = -w_{kc-1} \tag{4.14}$$

$$P_{kc+1} = P_{kc-1} \tag{4.15}$$

## CHAPTER V

### Formulation and implementation of the Numerical Algorithm

### 5.1 Objectives and requirements.

A concise review of the assumptions and objectives is perhaps in order before embarking upon the development of the algorithm. The governing equations are the Navier-Stokes equations in their non-conservative forms. The Poisson pressure equation derives from considerations of strict conservation of mass; the unconditional satisfaction of continuity, in effect, furnishing a causal connection linking the pressure to the velocities at each temporal state.

A fully implicit algorithm for solving for the flow variables is obtained by means of Backward-Time-Central-Space (BTCS) finite differencing of derivatives in the transformed plane, thus replacing the stability criteria with the less stringent convergence criteria. All difference equations apply at the point denoted by the space subscripts (i,j,k) and the time superscript (n). These subscripts and superscripts are occasionally omitted for reasons of convenience on the stipulation that they are understood to be present in all difference equations.

The final set of simultaneous algebraic equations is solved by a point SOR matrix iterative technique. Special numerical considerations and computational adjustments will be discussed in their proper contexts.

### 5.2 Coordinate transformations and finite difference approximations.

The spatial derivatives in the governing equations (3.15 - 3.17), in the physical plane are now to be transformed in order to yield the

transformed equations valid on a rectangular field with square grid in the computational plane. For the sake of conciseness of the equations, terms such as $u_x$, $v_y$, etc. will continue to appear in the text but are to be implicitly assumed to have been evaluated according to the relations and definitions given in Appendix A, as well as approximated by appropriate finite-difference expressions. The $\nabla^2( )$ terms in the momentum and pressure equations are, however, expanded into their transformed expressions for a specific purpose to be explained in due course. The transformed u-momentum has the following form:

$$u_t + uu_x + vu_y + wu_z = - P_x + \frac{\mu}{R_e J^2} (\alpha u_{\xi\xi} + \beta u_{\eta\eta} + \gamma u_{\xi\xi} + \delta u_{\xi\eta} + \sigma u_{\xi} + \tau u_{\eta} + \phi u_{\zeta}) + \frac{1}{R_e} [2\mu_x u_x + \mu_y (u_y + v_x) + \mu_z (w_x + u_z)] \qquad (5.1)$$

Similar expressions result for the v, w - momentum equations and the Poisson pressure equation.

Space and time derivatives in the transformed Navier-Stokes and pressure equations must be approximated by appropriate finite difference quotients on the discrete mesh system. For example, the following three-point second-order-accurate central difference approximations are used for subsequent numerical computations:

$$\left.\frac{\partial f}{\partial \xi}\right|_{i,j,k} = \frac{f_{i+1,j,k} - f_{i-1,j,k}}{2\Delta\xi} + O(\Delta\xi^2) \qquad (5.2)$$

$$\left.\frac{\partial^2 f}{\partial \xi^2}\right|_{i,j,k} = \frac{f_{i+1,j,k} - 2f_{i,j,k} + f_{i-1,j,k}}{\Delta\xi^2} + O(\Delta\xi^2) \qquad (5.3)$$

with analogous formulae for the $\eta$ and $\xi$ derivatives. It is to be noted that $\Delta\xi$ appearing in equations (5.2) and (5.3) is chosen to be unity by construction. Forward and backward three-point finite difference expressions were employed to approximate $\eta$-derivatives on the $\eta = 1$ and $\eta = \eta_{max}$ boundaries respectively while three-point forward expressions were used on the $\zeta = 1$ wall. These expressions, as well as those for the cross-derivatives, are second-order-accurate expressions in wide and common use and will not be further elaborated upon.

The time derivatives are represented by first-order-accurate two-point backward finite difference approximations at the first step in time after starting from rest and a second-order, three-point backward approximation thereafter. The difference expressions are given below.

First-order backwards:

$$f_t^n = (-f^{n-1} + f^n)/\Delta t \tag{5.4}$$

Second-order backwards:

$$f_t^n = (f^{n-2} - 4f^{n-1} + 3f^n)/2\Delta t \tag{5.5}$$

## 5.3 The Navier-Stokes equations in difference form.

A procedure unique to the primitive-variable formulation was used to augment the implicit algorithm resulting from the BTCS method of finite differencing. The transformed $\nabla^2( )$ terms in the momentum equations were expanded into their finite difference forms and the diagonal terms, (those with i,j,k as the spatial subscripts) were separated from their off-diagonal counterparts. The diagonal terms were then combined with a time-derivative term to form the diagonal elements of the matrix representation of the simultaneous algebraic equations. The procedure

is best illustrated by performing the manipulation on equation (5.1). The first term in parentheses on the right hand side of equation (5.1) represents $\nabla^2 u$ multipiied by a coefficient. Expansion of the derivatives $u_{\xi\xi}$, $u_{\eta\eta}$ and $u_{\zeta\zeta}$ into their finite difference forms result in the following expression for $\nabla^2 u$:

$$\nabla^2 u = \frac{1}{J^2}(\alpha u_{\xi\xi} + \beta u_{\eta\eta} + \gamma u_{\zeta\zeta} + \delta u_{\xi\eta} + \sigma u_{\xi} + \tau u_{\eta} + \phi u_{\zeta})$$

$$= \frac{1}{J^2}[\alpha(u_{i+1,j,k} - 2u_{i,j,k} + u_{i-1,j,k})$$

$$+ \beta(u_{i,j+1,k} - 2u_{i,j,k} + u_{i,j-1,k})$$

$$+ \gamma(u_{i,j,k+1} - 2u_{i,j,k} + u_{i,j,k-1})$$

$$+ \delta u_{\xi\eta} + \sigma u_{\xi} + \tau u_{\eta} + \phi u_{\zeta}]$$

$$= \frac{1}{J^2}\underbrace{-[2\alpha + 2\beta + 2\gamma)u_{i,j,k}]}_{\text{Diagonal}}$$

$$+ \frac{1}{J^2}\underbrace{[\alpha(u_{i+1,j,k} + u_{i-1,j,k}) + \beta(u_{i,j+1,k} + u_{i,j-1,k})}_{\text{Off - diagonal}}$$

$$+ \underline{\gamma(u_{i,j,k+1} + u_{i,j,k-1})}$$

$$+ \delta u_{\xi\eta} + \sigma u_{\xi} + \tau u_{\eta} + \phi u_{\zeta}] \qquad (5.6)$$

The time-derivative on the left hand side yields one term involving $u^n$ on the left hand side and after some rearrangement of terms the desired form of the u-momentum equation is obtained as

$$u^n[\frac{A}{\Delta t} + \frac{\mu}{R_e J^2}(2\alpha + 2\beta + 2\gamma)] = -(uu_x + vu_y + wu_z) - P_x + \frac{\mu}{R_e J^2}[\alpha(u_{i+1,j,k}$$

$$+ u_{i-1,j,k}) + \beta(u_{i,j+1,k} + u_{i,j-1,k}) + \gamma(u_{i,j,k+1,} + u_{i,j,k-1})$$

$$+ \delta u_{\xi\eta} + \sigma u_{\xi} + \tau u_{\eta} + \phi u_{\zeta}]$$

$$+ \frac{1}{R_e}[2\mu_x u_x + \mu_y(u_y + v_x) + \mu_z(w_x + u_z)] + B_1 \qquad (5.7)$$

where,

$$A = 1$$

for first-order backwards time-differencing.

$$B_1 = \frac{u^{n-1}}{\Delta t} \qquad (5.8)$$

and

$$A = \frac{2}{3}$$

for second-order backwards time-differencing

$$B_1 = \frac{1}{2\Delta t}(4u^{n-1} - u^{n-2}) \qquad (5.9)$$

v and w-momentum equations, developed after a similar fashion, are:

$$v^n[\frac{A}{\Delta t} + \frac{\mu}{R_e J^2}(2\alpha + 2\beta + 2\gamma)] = -(uv_x + vv_y + wv_z)$$

$$+ P_y + \frac{\mu}{R_e J^2}[\alpha(v_{i+1,j,k} + v_{i-1,j,k}) + \beta(v_{i,j+1,k} + v_{i,j-1,k})$$

$$+ \gamma(v_{i,j,k+1} + v_{i,j,k-1}) + \delta v_{\xi\eta} + \sigma v_{\xi} + \tau v_{\eta} + \phi v_{\zeta}]$$

$$+ \frac{1}{R_e}[2\mu_y v_y + \mu_z(v_z + w_y) + \mu_x(u_y + v_x)] + B_2 \qquad (5.10)$$

and,

$$w^n[\frac{A}{\Delta t} + \frac{\mu}{R_e J^2}(2\alpha + 2\beta + 2\gamma)] = -(uw_x + vw_y + ww_z) - P_z$$

$$+ \frac{\mu}{R_e J^2}[\alpha(w_{i+1,j,k} + w_{i-1,j,k}) + \beta(w_{i,j+1,k} + w_{i,j-1,k})$$

$$+ \gamma(w_{i,j,k+1} + w_{i,j,k-1} + \delta w_{\xi\eta} + \sigma w_{\xi} + \tau w_{\eta} + \phi w_{\zeta}]$$

$$+ \frac{1}{R_e}[2\mu_z w_z + \mu_x(w_x + u_z) + \mu_y(w_y + v_z)] + B_3 \qquad (5.11)$$

$B_2$ and $B_3$ are obtained by substituting u with v and w respectively in definitions (5.8) and (5.9).

## 5.4 The pressure equation.

The difference form of the Poisson pressure equations is obtained by performing the operation described in article 5.3 on the $\nabla^2 P$ term in equation (3.19). The term $D_t$ represents the time-derivative of the divergence of the velocity vector. Using a two-point backward difference approximation for $D_t$ and noting that $D^n = 0$ as dictated by the requirement for preservation of continuity, the Poisson pressure equation is rewritten as,

$$\frac{1}{J^2}(2\alpha + 2\beta + 2\gamma)P_{i,j,k} = u_x^2 + v_y^2 + w_z^2 + 2v_x u_y + 2w_x u_z + 2w_y v_z$$

$$+ \frac{1}{J^2}[\alpha(P_{i+1,j.k} + P_{i-1,j,k}) + \beta(P_{i,j+1,k} + P_{i,j-1,k})$$

$$+ \gamma(P_{i,j,k+1} + P_{i,j,k-1}) + \delta P_{\xi\eta} + \sigma P_{\xi} + \tau P_{\eta} + \phi P_{\zeta}]$$

$$- \frac{2}{R_e}[\mu_x \nabla^2 u + \mu_y \nabla^2 v + \mu_z \nabla^2 w + \mu_{xx} u_x + \mu_{yy} v_y + \mu_{zz} w_z$$

$$+ \mu_{xy}(u_y + v_x) + \mu_{zx}(w_x + u_z) + \mu_{zy}(v_z + w_y)] - \frac{D^n - 1}{\Delta t} \qquad (5.12)$$

## 5.5 Difference equations for boundary conditions.

Pressure values on impermeable surfaces in the flow are determined by extrapolation from the field subject to the Neumann boundary conditions delineated in article 4.2. $P_{\eta}$ or $P_{\zeta}$ in equations (4.7 - 4.8) are

evaluated on the surfaces by three-point backward or forward difference approximations as the case may be, depending on the location of the surface with respect to the coordinate system.

The $\eta = 1$ boundary is congruent in part with the airfoil; therefore $\eta$-derivatives on the airfoil are of necessity to be approximated by forward differences. Along a similar line of reasoning, the top and the bottom walls ($\eta = \eta_{max}$), are seen to require backward $\eta$-differencing while the end-wall ($\zeta = 1$) requires forward $\zeta$-differencing.

The resulting expressions for boundary pressure on the various solid boundaries are:

On the airfoil,

$$P_{i,1,k} = -\frac{1}{3}P_{i,3,k} + \frac{4}{3}P_{i,2,k} - \frac{2}{3}\frac{1}{\gamma_c}\left[P_\xi \beta_c + J_c(g_2 x_\xi - g_1 y_\xi)\right] \tag{5.13}$$

On the top and the bottom walls,

$$P_{i,JMAX,k} = -\frac{1}{3}P_{i,JMAX-2,k} + \frac{4}{3}P_{i,JMAX-1,k} + \frac{2}{3}\frac{1}{\gamma_c}\left[P_\xi \beta_c + J_c(g_2 x_\xi - g_1 y_\xi)\right] \tag{5.14}$$

On the end-wall ($\zeta = 1$),

$$P_{i,j,1} = \frac{1}{3}P_{i,j,3} + \frac{4}{3}P_{i,j,2} = F'(\zeta) g_3 \tag{5.15}$$

## 5.6 Special considerations and computational adjustments.

### 5.6.1 Finite differencing on the reentrant sections.

The procedure for the application of finite difference approximations on the cut extending from the trailing edge of the airfoil to the outflow section in a C-type grid is rather extraordinary and

deserves special attention. The two reentrant sections, $\Gamma_5$ and $\Gamma_6$ (fig. 1), resulting from the cut are one and the same line in the physical plane, albeit ostensibly separated from each other in the transformed computational plane. Any point on the segment $\Gamma_5$ is congruent with a corresponding point on $\Gamma_6$, eg., the points designated by the indices (IMAX-1, 1) and (ITV + 1, 1) are indistinguishable in the physical plane from the points at (2,1) and (ITL - 1, 1) respectively with similar correspondence existing between all other points distributed between the trailing edge and the outflow boundary. These corresponding points, therefore, have the same x and y coordinate values inspite of the differences in their associated $\xi$-values. Evaluation of derivatives and flow calculations are necessary along only one of these reentrant sections since they carry the same values of the flow variables.

At a casual glance, the evaluation of derivatives on either of these sections by means of central-difference approximations may seem rendered impossible by the absence of a J - 1 line, since the reentrant sections correspond to the $\eta = 1$ line. A closer view of the physical geometry involved reveals, however, that the J = 2 line reemerging behind the trailing edge after circumscribing the airfoil, serves as a surrogate J - 1 line thus making central-differencing possible while ensuring satisfaction of the strict requirement for continuous derivatives across the cut. The resulting central-difference expressions for the derivatives across the cut at the points corresponding to I = I1 and I = I2 (figure 1) are given below.

$$(f_\eta)_{I1,1} = (f_\eta)_{I2,1} = (f_{I1,2} - f_{I2,2})/2 \qquad (5.16)$$

$$(f_{\eta\eta})_{I1,1} = (f_{\eta\eta})_{I2,1} \simeq f_{I1,2} - 2f_{I1,1} + f_{I2,2} \tag{5.17}$$

$$(f_{\xi,\eta})_{I1,1} = (f_{\xi\eta})_{I2,1} \simeq (f_{I1-1,2} - f_{I1+1,2} + f_{I2+1,2} - f_{I2-1,2})/4 \tag{5.18}$$

where,

$I2 = IMAX - (I1 - 1)$

The k-index has been omitted for reasons for simplicity.

5.6.2 Artifical viscosity.

Extraneous oscillations contaminating the solution, eg., those arising out of inaccuracies introduced by finite differencing, may lead to instability and ultimately divergence of the solution particularly at high Reynolds numbers. An artificial viscosity, judiciously used, can diffuse these nonphysical instabilities and save the solution from being overcome by violent oscillations.

Since the preservation of continuity is an underlying stipulation in the solution scheme, an unusually high magnitude of the divergence $\nabla \cdot \underset{\sim}{u}$ of the velocity vector should be symptomatic of spurious oscillations in the dependent variables. Based on this reasoning an artificial viscosity coefficient, [14], designed to be proportional to the magnitude of $\nabla \cdot \underset{\sim}{u}$, is appended to the viscosity coefficient in the momentum equations (3.15 - 3.17). The coefficient $\mu$ is therefore composed of three parts as shown below,

$$\mu = 1 + \varepsilon + \vartheta \tag{5.19}$$

where,

$\varepsilon$ accounts for the turbulent eddy viscosity

and

$\vartheta$ represents the artificial viscosity being discussed here

$\theta$ is being defined as

$$\theta = \lambda R_e J |\nabla \cdot \underset{\sim}{u}| \tag{5.20}$$

where $\lambda \geq 0$ and J is the Jacobian of the coordinate transformation.

The artificial viscosity $\theta$ can be perceived to have the dual sought-after attributes of coming into play only where $\nabla \cdot \underset{\sim}{u}$ is undesirably high and of being proportional to the magnitude $|\nabla \cdot \underset{\sim}{u}|$ at the same time. Suitably chosen values of $\lambda$ can limit the effects of the artificial viscosity.

## 5.7 A brief outline of computational sequences.

The wing, the wind-tunnel and the associated coordinate system are started from rest and accelerated to the ultimate free-stream velocity. The free-stream velocities are distributed in time along a cosine curve of the following form,

$$\begin{aligned} U_\infty &= \frac{1}{2}[1 + \cos\pi\ (t + 1)] \quad 0 \leq t < 1 \\ U_\infty &= 1 \text{ for } t \geq 1 \end{aligned} \tag{5.21}$$

At each time-step the boundary values of pressure and the velocities are applied to the various boundaries occurring in the flow prior to each iteration. One iteration of the SOR iterative method is then performed. Appropriate optimum acceleration parameters $\omega$, are calculated as described in Appendix B, and used to update the successive iterates according to the following formula.

$$f^{(s+1)} = \omega \bar{f}^{(s+1)} + (1 - \omega) f^{(s)} \tag{5.22}$$

where f represents any one of the three dependent variables u, v and

$\omega$, while the superscript (s) denotes the iterations counter. The pressure solution is not accelerated. The unaccelerated Gauss-Seidel iterate is represented by $\bar{f}$.

The Navier-Stokes and the pressure equations are solved simultaneously in the field to maintain the implicit characteristic of the algorithm. Iteration and evaluation of boundary conditions are alternated until a desired degree of convergence is achieved at the current time level. The free-stream is then accelerated to the next step in time, the boundary values are calculated and a new set of iterations commence. This procedure is continued until a steady state solution results.

## CHAPTER VI

## Computational Results

### 6.1 Coordinate Systems

Coordinate grids were generated for symmetric NACA airfoils for a range of Reynolds numbers by means of the boundary-fitted schemes of Thompson [2] and Sorenson [3]. The airfoils used were the NACA 0012 and NACA $66_3018$ sections. Field sizes of the computational grids varied with variations in the Reynolds number and the shape of the airfoil used.

In the Reynolds number range of 1000-10,000, each two-dimensional grid contained 49 x 22 points describing the field geometry, with five such grids placed along the span at stations including the side-wall and the post-midspan section. In other words, there were 49 constant-$\xi$ lines and 22 constant-$\eta$ lines defining each discrete two dimensional mesh.

For $R_e$ = 40,000, the two dimensional field size was increased to 55 x 31 to accommodate the intensified requirements for resolution of the boundary layers. The number of spanwise stations was increased to 20 keeping in view a proposed project involving the resolution of the boundary layer near the side-wall at high Reynolds numbers.

Coordinate lines were concentrated in the boundary layers, the first line away from the surface being located at a distance of one percent of the calculated thickness of the boundary layer on a flat plate.

The computational results presented in this dissertaion were obtained from computations performed on grids generated by Sorenson's

'GRAPE' code, although grid generation techniques of both Thompson and Sorenson were experimented with. Figures 4 - 7 present the coordinate systems for the particular flow situations investigated. In all these coordinate grids the chord of the airfoil lies midway between the top and the bottom walls of the wind tunnel along the y = 0 line with the leading edge at x = 0, and the trailing edge at x = 1. The top and the bottom walls correspond to y = 2, and y = -2 lines and have their leading and trailing edges at x = -1 · 0, and x = 4 · 0 respectively. The span extends from z = 0 to z = 2, so that the side-wall corresponds to the z = 0 plane while the midspan section is situated at z = 1.

## 6.2 Results for NACA 0012 Airfoil

### 6.2.1 Results for $R_e$ = 1000 and A = 0°

Relevant flow conditons governing this part of the computations are:

$R_e = 1000$

$A = 0°$

$\theta = 0$; $\lambda = 0$

$\varepsilon$ : Computed

The turbulent eddy viscosity $\varepsilon$, though inappreciably small in magnitude at this low Reynolds number, was included in these computations but was quiescent as might be expected. The use of the artificial viscosity $\theta$ was neither warranted nor necessary since no instability was encountered in the solution. $\theta$ was set equal to zero by using a zero value for the coefficient $\lambda$.

Distributions of $C_p$, the pressure coefficient are presented at two time levels - t = 1.0 and t = 2.0. The transient states of the

solutions, though unimportant from the point of view of practical utility, are presented to demonstrate the time-dependence of the solution. Figures 8-11 show the $C_p$ distributions at t = 1.0, i.e., after the solution has advanced through 100 time steps, each .01 in magnitude. $C_p$ distributions in figures 12-15 are those at t = 2.0. A distinct change in the pressure profiles is noticed particularly near the leading and the trailing edges. The differences between the pressure values on the upper and the lower surfaces are seen to have considerably lessened. These discrepancies arise out of inadequate resolution of the flow quantities at regions containing large gradients and are attributable in part to an insufficient number of points in the discrete mesh.

Velocity profiles around the airfoil are represented in figures 16-19, while figures 20-23 show the distribution of velocities along constant-$\xi$ lines bridging the gap between the airfoil and the top wall of the wind tunnel. Well developed boundary layers are noticed at both surfaces.

Resolution of the boundary layer adjacent to the side-wall ($\zeta$ = 1) was not attempted, the number of spanwise grids being limited by considerations of affordability of computer storage. However, pressure profiles do vary along the span as is evident upon examination of the $C_p$ distributions at different values of the index k. Little or no change was noticed in the pressure distributions on the top and the bottom walls with change in the value of k, and the $C_p$ distributions at k = 4 are presented in figures 24 and 25.

The solution reached a reasonable degree of convergence and was considered to have demonstrated a proper qualitative trend at t = 2.0

where the calculations were terminated.

### 6.2.2 Results for $R_e$ = 1000 and A = 12°

The coordinate system shown in Figure 5 was used in this part of the computations. The relevant flow parameters were,

$R_e$ = 1000

A = 12°

$\theta$ = 0; $\lambda$ = 0

$\varepsilon$ : computed

A great deal of computation-time was saved in this case by starting the solution from the steady-state solution obtained in the case of zero-angle-of-attack described in the previous section.

Velocity profiles at the midspan section (k = 4) are presented in Figures 26 and 27 at 5 and 60 time-steps after restart respectively. The beginnings of a vortex, arising out of the sudden rotation of the airfoil, is discernible at the trailing edge; nevertheless, the solution scheme demonstrates remarkable adaptability and the flow soon settles down. The velocities follow the contours properly and a stable solution is obtained as shown in Figure 27.

Pressure coefficient distributions along the span are presented in Figures 28-31 and generally agreeable qualitative trends are observed.

## 6.3 Results for NACA $66_3018$ airfoil section.

### 6.3.1 Results for $R_e$ = 10,000 and A = 0°

The governing parameters are:

$R_e$ = 10,000

A = 0

$\lambda = 1.0$

$\epsilon$ : computed

This phase of the computation was performed on the mesh shown in Figure 6. The solution was restarted using the steady state solution obtained with the NACA 0012 airfoil described in section 6.2.1, as an inital guess.

As the solution progressed in time the pressure went through phases of development and finally settled to a steady profile after 90 time steps. Figures 32-34 present the temporal evolution of the pressure distribution on the airfoil at the k = 4, station, as the flow strived to conform to the suddenly imposed changes in geometry and Reynolds number. Comparing the results with those obtained in the case of the NACA 0012 airfoil at A = 12°, the change in the Reynolds number seemed to be the harder obstacle to overcome. The artificial viscosity was brought into effect by setting $\lambda = 1$. $C_p$ - distributions at various spanwise stations on the airfoil are presented in figures 35-38.

Experimental results obtained by Mueller [15], from wind-tunnel tests of the NACA $66_3018$ airfoil at a Reynolds number of 40,000 are plotted along with the computational results for $R_e$ = 10,000, in Figure 39. Since the Reynolds numbers of the results being compared are different, no degree of quantitative exactitude of replicability was sought. The comparison was performed in the hope of establishing that the computed pressures do duplicate the general qualitative trends of the experimental results and this assertion seems to have been borne out by the plotted comparison.

The lack of a substantial degree of steepness in the pressure profile at the leading edge is attributable in part to insufficiency of the number of grid points available in this region of sharp gradients in flow variables. The trailing edge pressure, however, drops with time and indicates a promise of following the trend set by the experimental results.

The velocity profiles on the surface of the airfoil at the mid-span section are presented in Figure 40. The boundary layer is seen to be well developed. The apparent penetration of the nose of the airfoil by the fluid resulted from the abrupt changes in geometry and Reynolds number compounded with altered grid spacing in the boundary layer as well as the inadequacy of the number of η-lines available near the surface in properly resolving the boundary layer. Continued advance in time did not get rid of this abnormality.

## CHAPTER VII

### Discussions and Conclusions.

The implicit algorithm employed in this research to compute the flow about an airfoil spanning a wind tunnel does live up to most of the researcher's expectations although the absence of quantitative comparison of results leave some things to be desired.

A scrutiny of the presented computational results indicates that an algorithm with substantially stable characteristics is at work. The stability, expected of a fully implicit algorithm, asserts itself, particularly in the case of the NACA 0012 airfoil at an angle of attack of 12 degrees. Despite restarting the solution from the steady state obtained with zero angle of attack, the flow soon attains conformity with the changed geometric configuration. The front stagnation point moves away from the leading edge to the adjacent point on the lower surface of the airfoil, the streamlines follow the contours and the pressure builds up on the upper surface while dropping on the lower surface. The flow demonstrates similar, if not as spectacular, adaptability in the case of the NACA $66_3018$ airfoil with $R_e = 10{,}000$. The results, therefore, are encouraging enough to warrant planning the use of the algorithm in future computations at higher Reynolds numbers.

Proper resolution of a flow field is directly dependent on the number of grid points available in the field. It was in this crucial area that the research was constrained by the limits of affordability of computer storage and hence the number of discrete mesh points. The storage requirements and the computation time for a complete three dimensional solution are truly overwhelming and consequently it was

deemed prudent to limit the field size to one just large enough to make it possible to ascertain the qualitative characteristics of the solution.

Some of the relevant computational parameters should be made note of here. The number of iterations for each time-step was limited to a maximum of 20. Further iterations did not seem to significantly enhance convergence. Typical error norms after 20 iterations were of the order of $10^{-4}$. With a total of 49 x 22 x 5 points in the three-dimensional computational space, an average of 50.0 seconds of computer time per time-step was expended on the CDC CYBER 175 machine. The storage requirements amounted to an approximate total of $3 \times 10_8^6$ locations. With a limit of 100K for the machine used, there was not sufficient free space left to enable an increase of the number of data points.

Among the forecasts for the future is a project already in progress, involving computations at realistically high Reynolds numbers, on a grid many times bigger and denser than the ones used in this research. The CDC CYBER 203 offers virtually unlimited storage capability and is the machine chosen for these future computations.

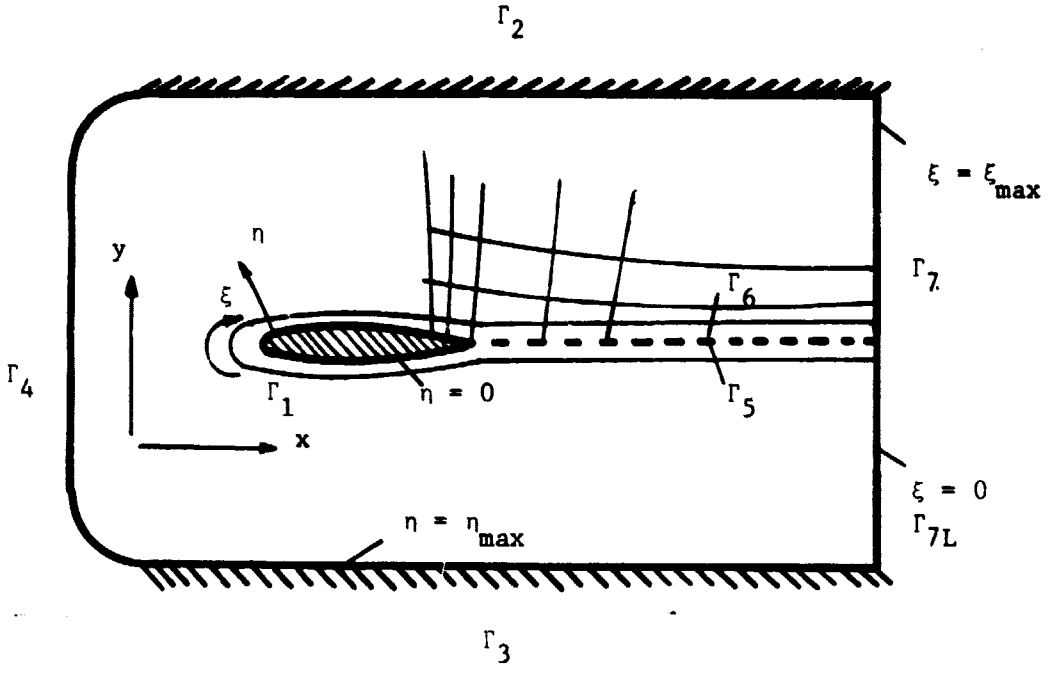


a. Physical Plane

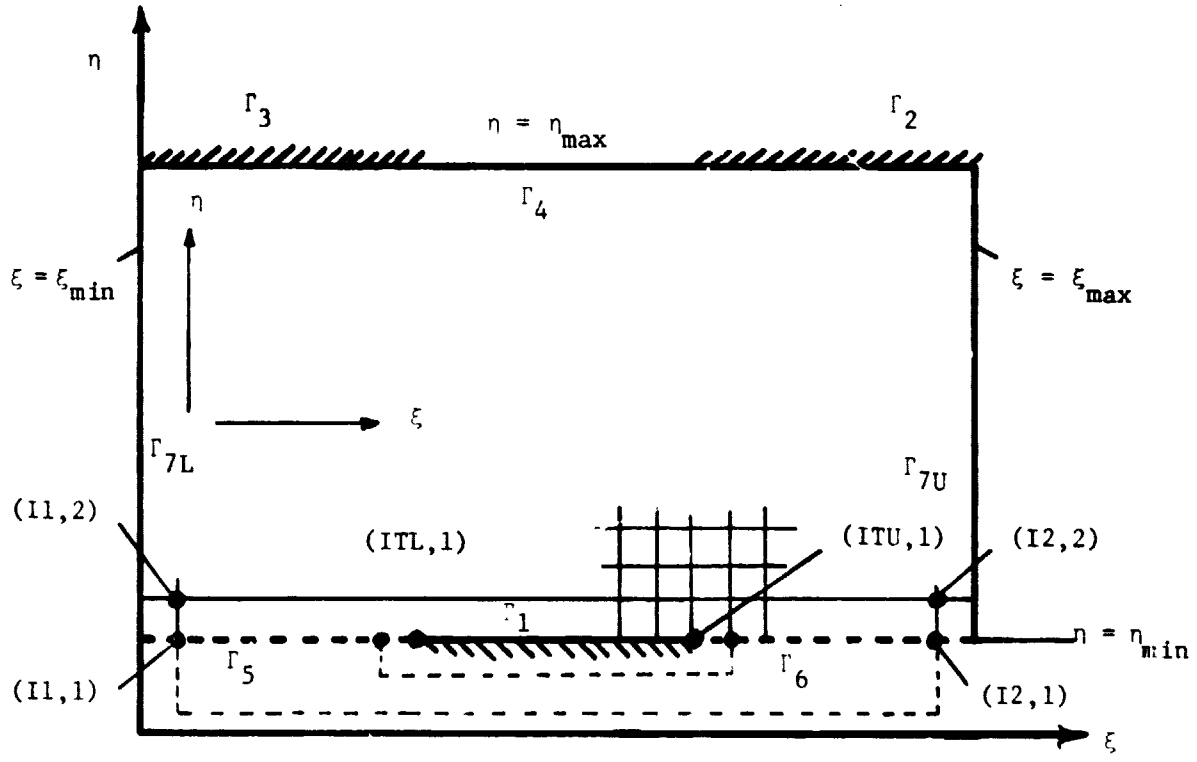


b. Transformed Plane

Figure 1. C-Type Coordinate System

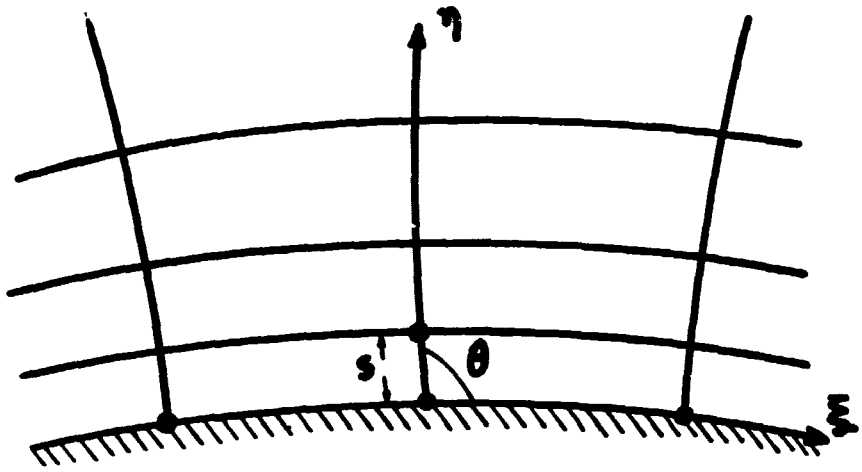


Figure 2. Coordinate Line Attraction Parameters

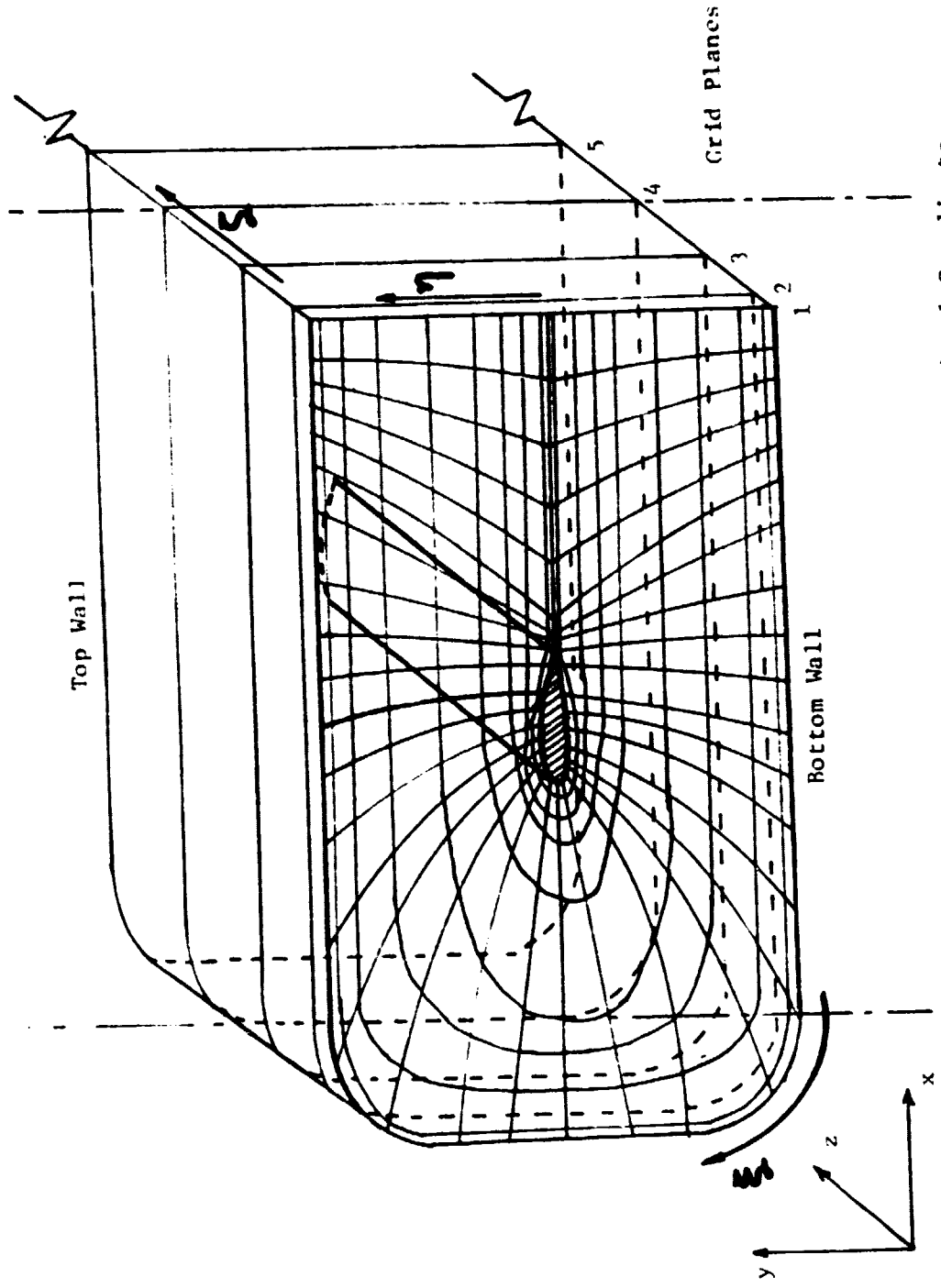


Figure 3. Schematic Diagram of Three-dimensional Coordinate System for Airfoil Spanning a Wind Tunnel

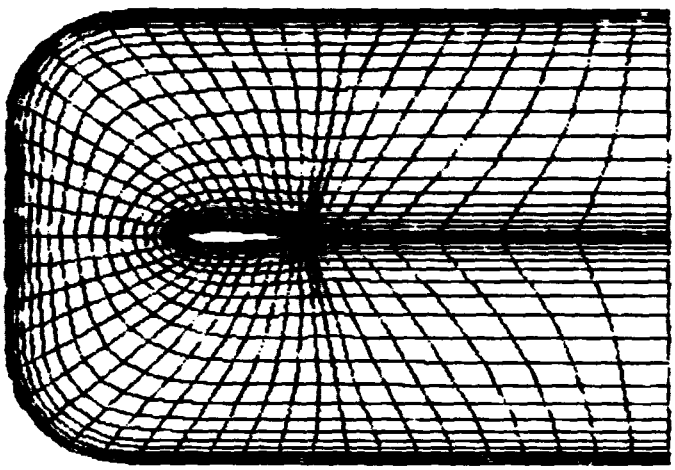

Figure 4. Coordinate System for NACA 0012 Airfoil - $R_e = 1000$, $A = 0^\circ$

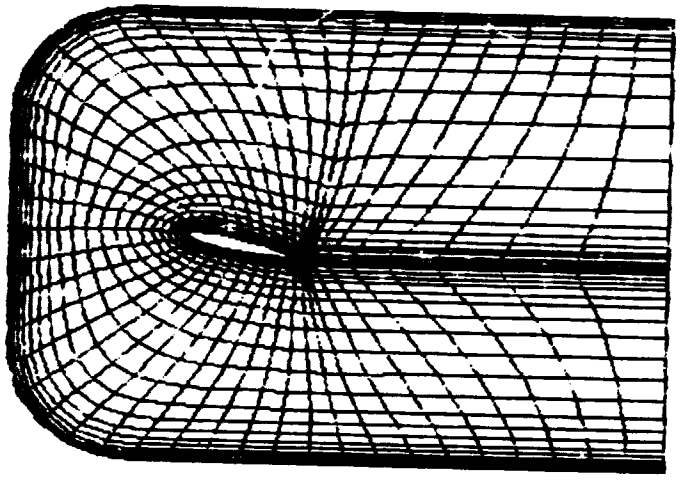

Figure 5. Coordinate System for NACA 0012 Airfoil - $R_e = 1000$, $A = 12°$

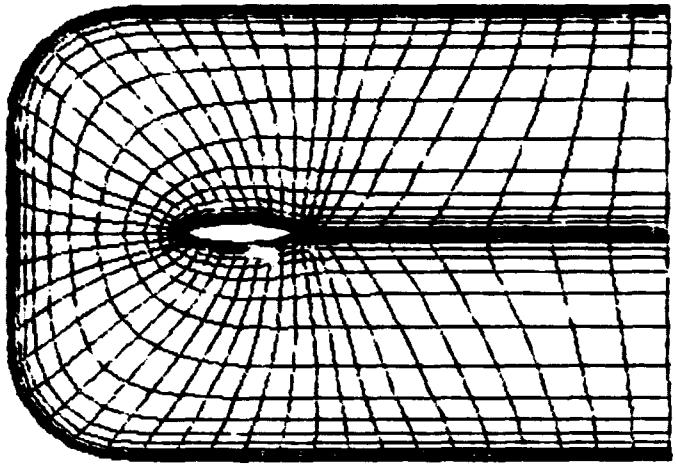

Figure 6. Coordinate System for NACA $66_3018$ Airfoil - $R_e$ = 10,000, A = 0°

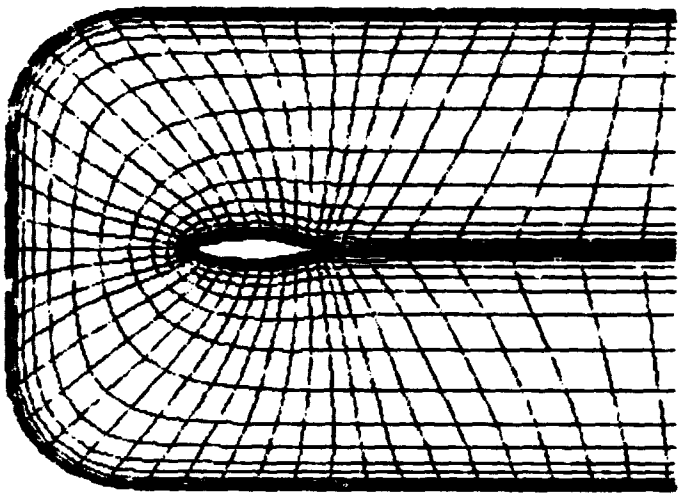

Figure 7. Coordinate System for NACA $66_3018$ Airfoil - $R_e = 40{,}000$, $A = 0°$

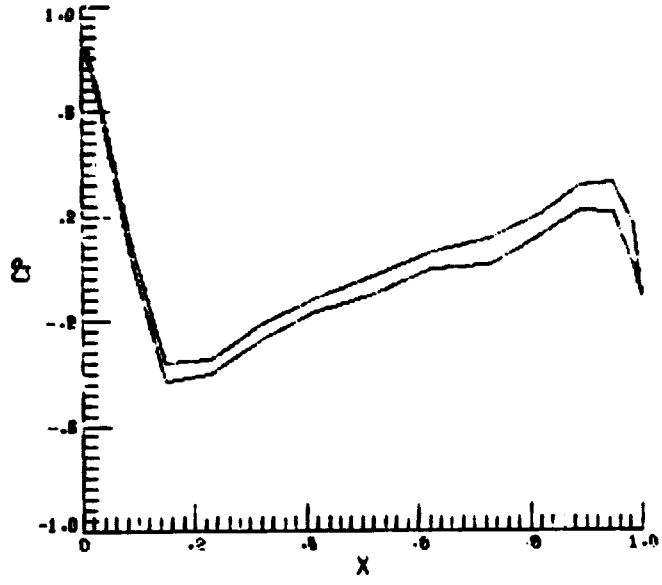


Figure 8. Pressure Distribution (NACA 0012) - $R_e$ = 1000, A = 0°, t = 1.0, k = 1 (wall)

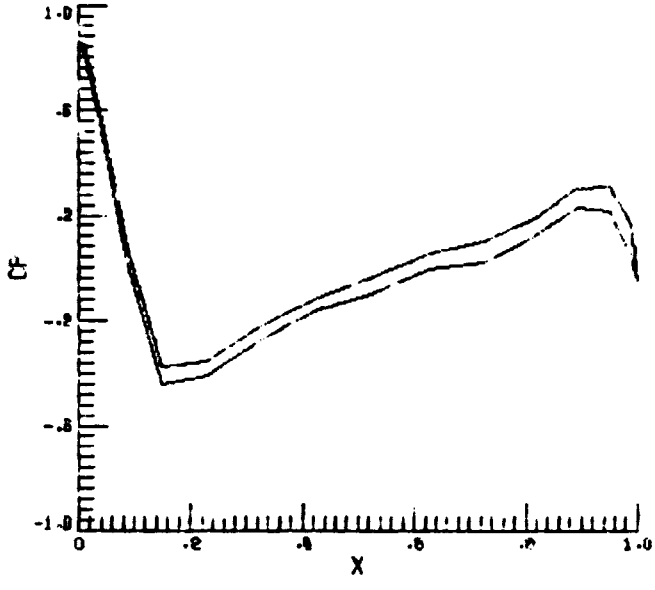


Figure 9. Pressure Distribution (NACA 0012) - $R_e$ = 1000, A = 0°, t = 1.0, k = 2

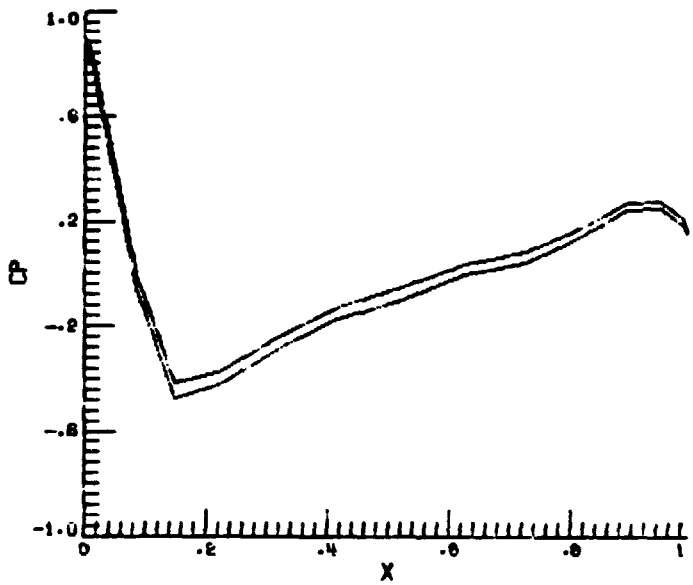


Figure 10. Pressure Distribtuion (NACA 0012) - $R_e$ = 1000, A = 0°, t = 1.0, k = 3

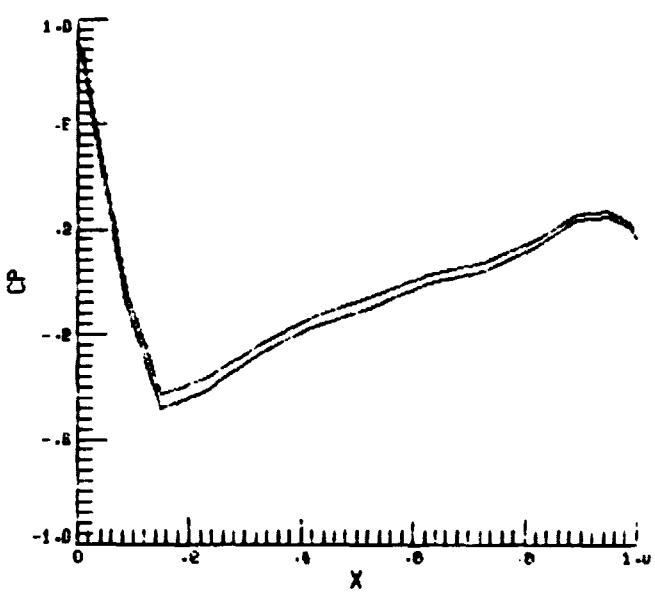


Figure 11. Pressure Distribution (NACA 0012) - $R_e$ = 1000, A = 0°, t = 1.0, k = 4 (midspan)

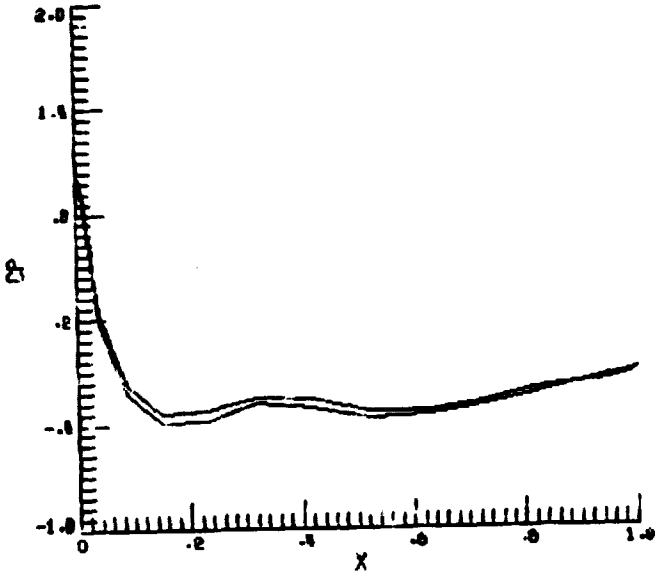


Figure 12. Pressure Distribution (NACA 0012) - $R_e$ = 1000, A = 0°, t = 2.0, k = 1 (wall)

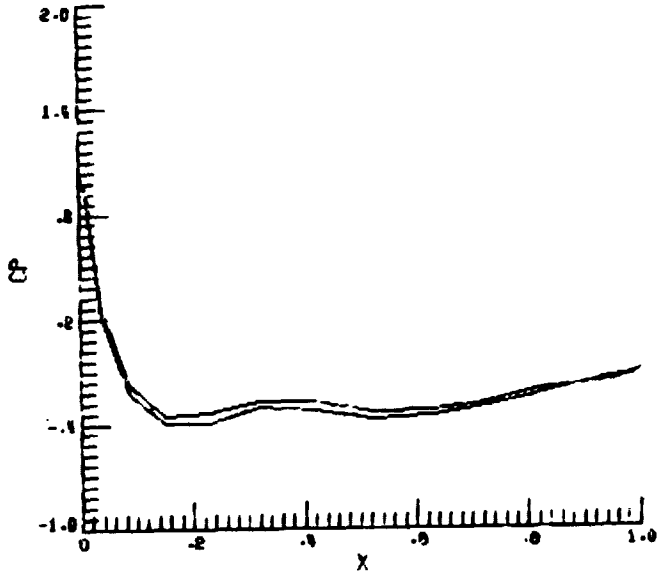


Figure 13. Pressure Distribution (NACA 0012) - $R_e$ = 1000, A = 0°, t = 2.0, k = 2

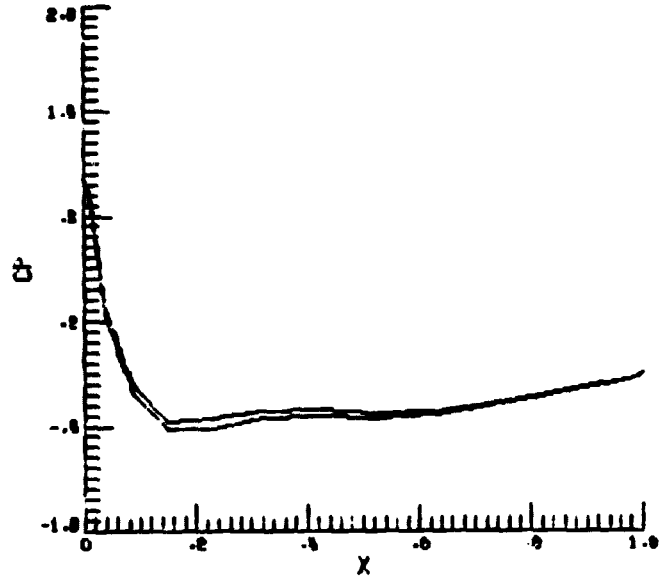


Figure 14. Pressure Distribution (NACA 0012) - $R_e$ = 1000, A = 0°, t = 2.0, k = 3

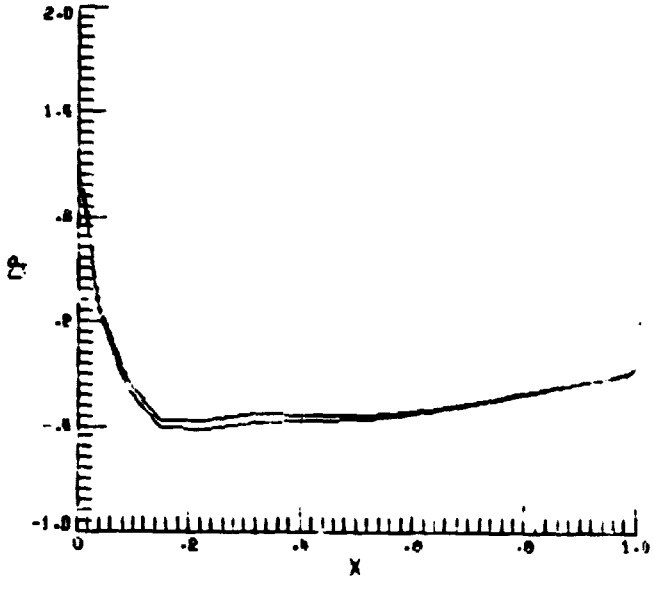


Figure 15. Pressure Distribution (NACA 0012) - $R_e$ = 1000, A = 0°, t = 2.0, k = 4 (midspan)

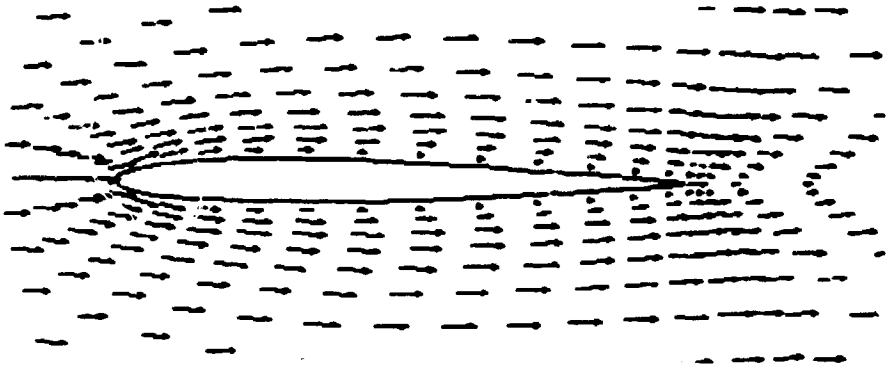

Figure 16. Velocity Profiles Around Airfoil (NACA 0012) - $R_e$ = 1000, A = 0°, t = 2.0, k = 2

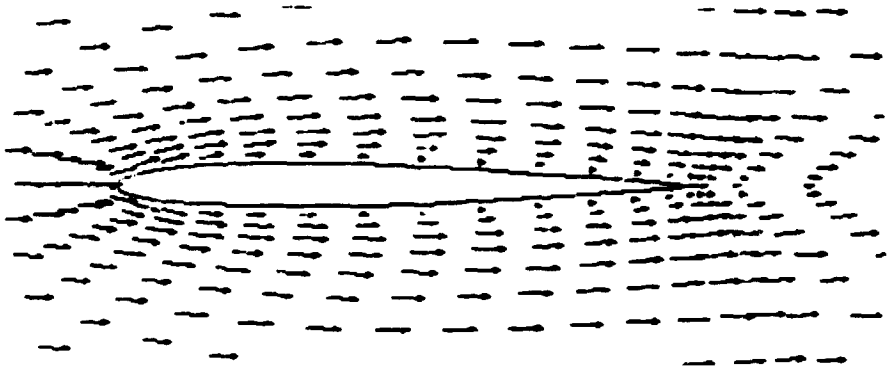

Figure 17. Velocity Profiles Around Airfoil (NACA 0012) - $R_e$ = 1000, A = 0°, t = 2.0, k = 3

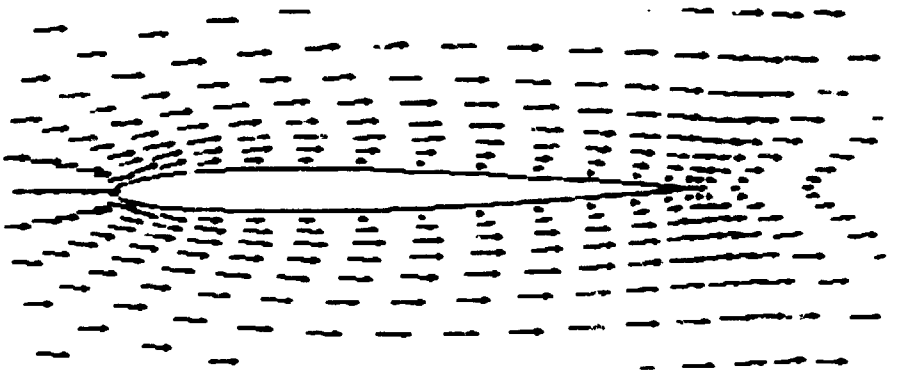

Figure 18. Velocity Profiles Around Airfoil (NACA 0012) - $R_e$ = 1000, A = 0°, t = 2.0, k = 4 (midspan)

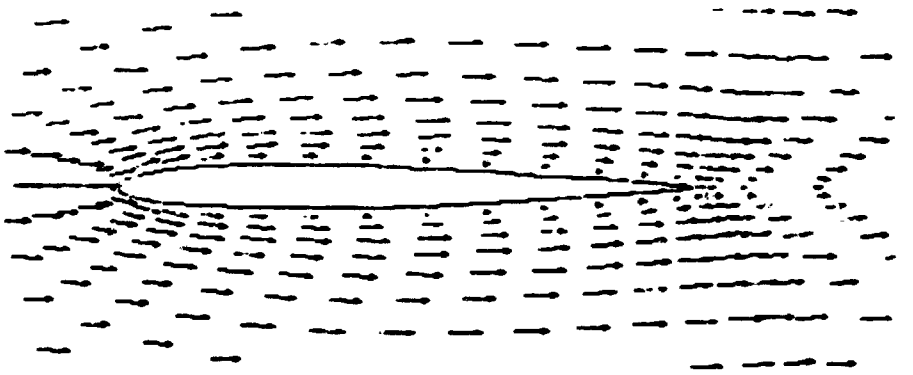

Figure 19. Velocity Profiles Around Airfoil (NACA 0012) - $R_e$ = 1000, A = 0°, t = 2.0, k = 5

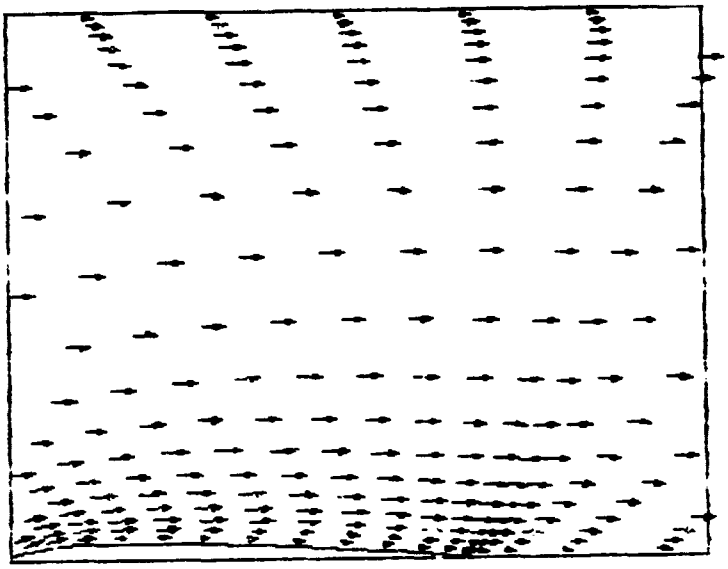

Figure 20. Velocity Distribution in Wind Tunnel (NACA 0012) - $R_e$ = 1000, A = 0°, t = 2.0, k = 2

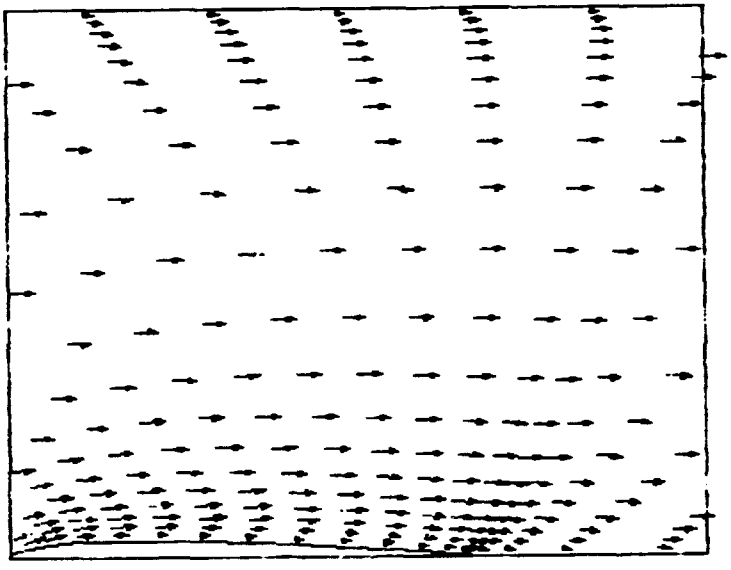

Figure 21. Velocity Distribution in Wind Tunnel (NACA 0012) - $R_e$ = 1000, A = 0°, t = 2.0, k = 3

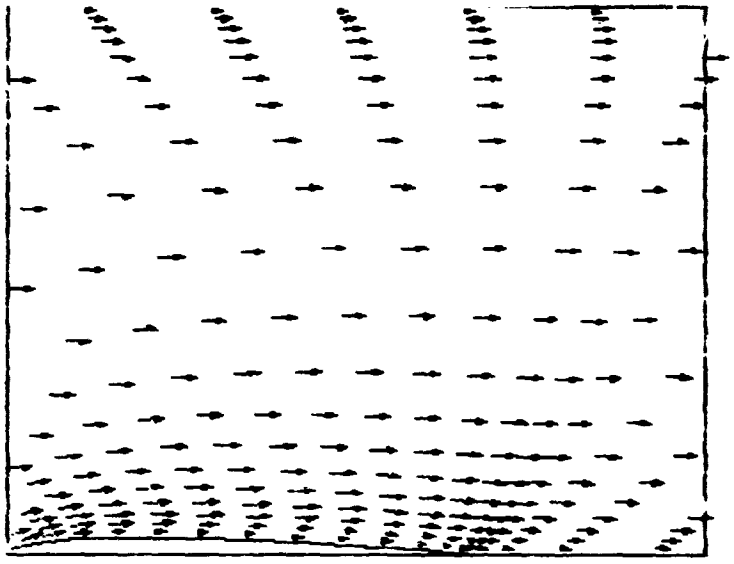

Figure 22. Velocity Distribution in Wind Tunnel (NACA 0012) - $R_e$ = 1000, A = 0°, t = 2.0, k = 4 (midspan)

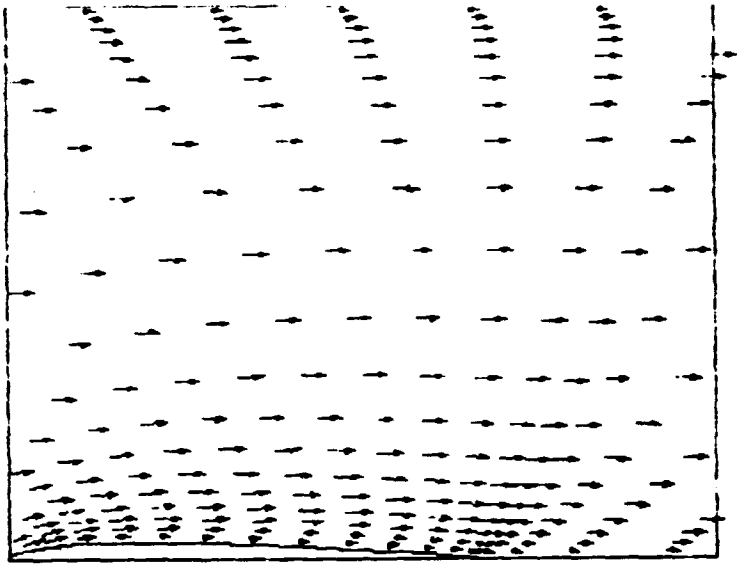

Figure 23. Velocity Distribution in Wind Tunnel (NACA 0021) - $R_e$ = 1000, A = 0°, t = 2.0, k = 5

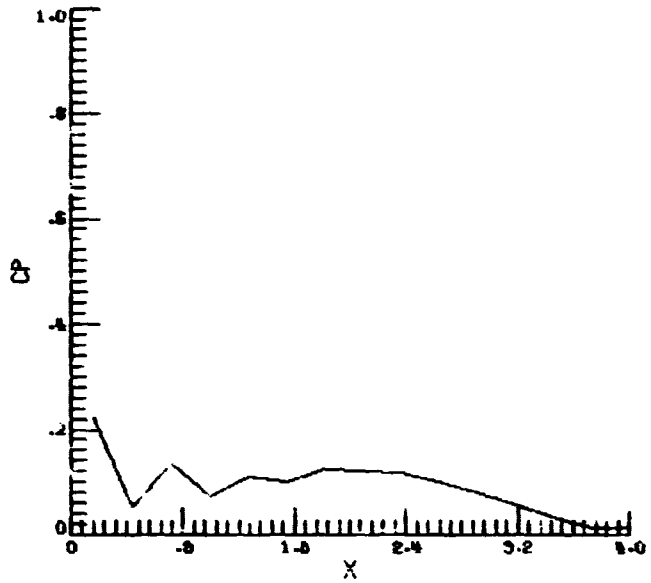


Figure 24. Pressure Distribution On The Top Wall - $R_e$ = 1000

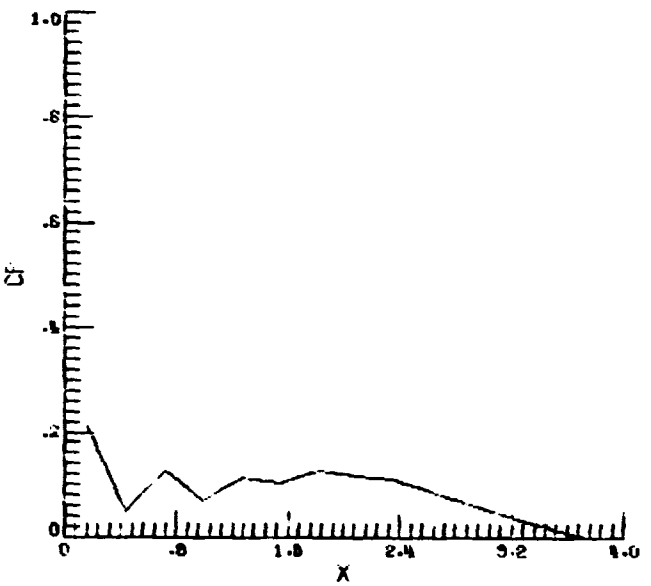


Figure 25. Pressure Distribution On The Bottom Wall - $R_e$ = 1000

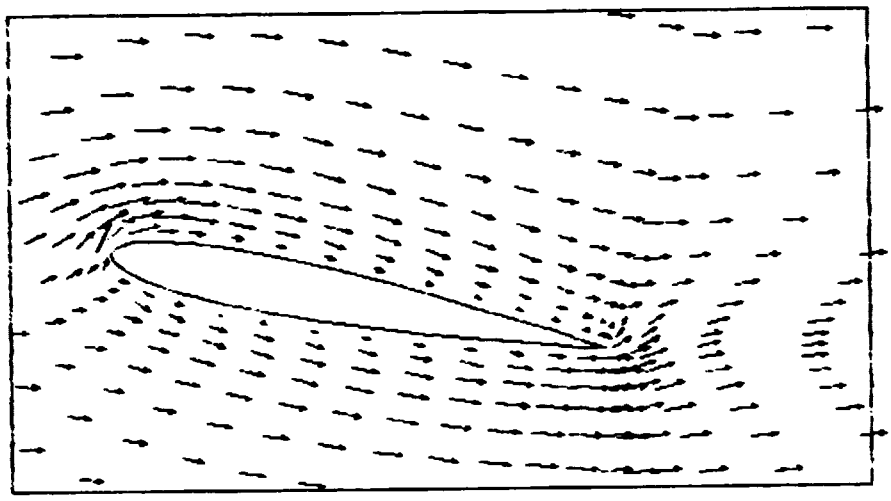

Figure 26. Velocity Profiles Around Airfoil (NACA 0012) - $R_e$ = 1000, A = 12°, t = 2.05, k = 4 (midspan)

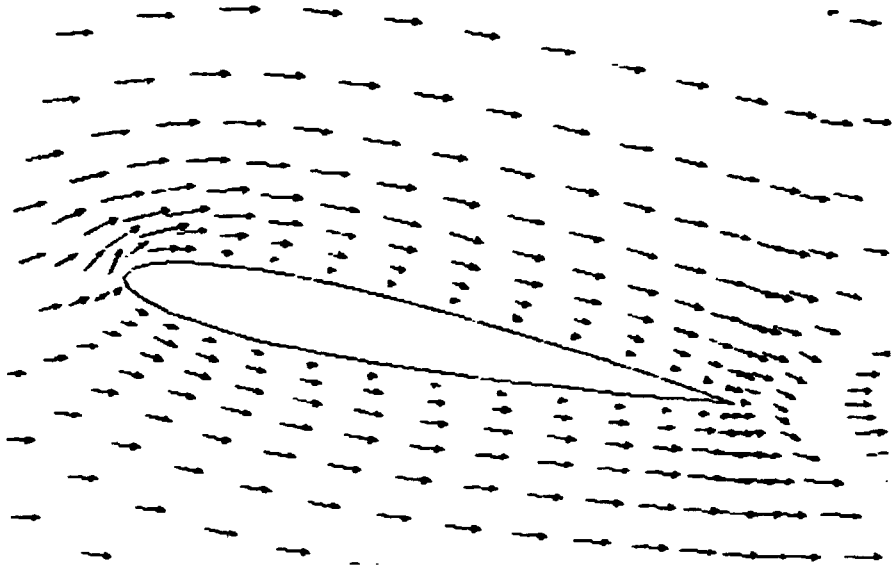

Figure 27. Velocity Profiles Around Airfoil (NACA 0012) - $R_e$ = 1000, A = 12°, t - 2.6, k = 4 (midspan)

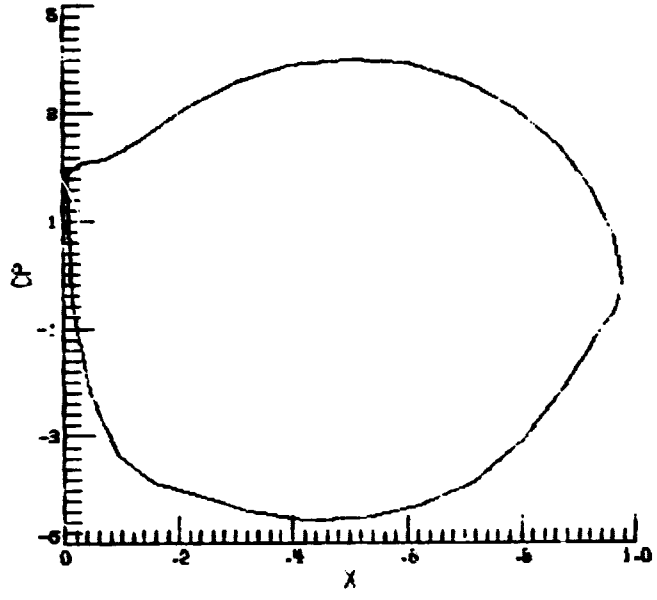


Figure 28. Pressure Distribution (NACA 0012) - $R_e$ = 1000, A = 12°, t = 2.05, k = 4 (midspan)

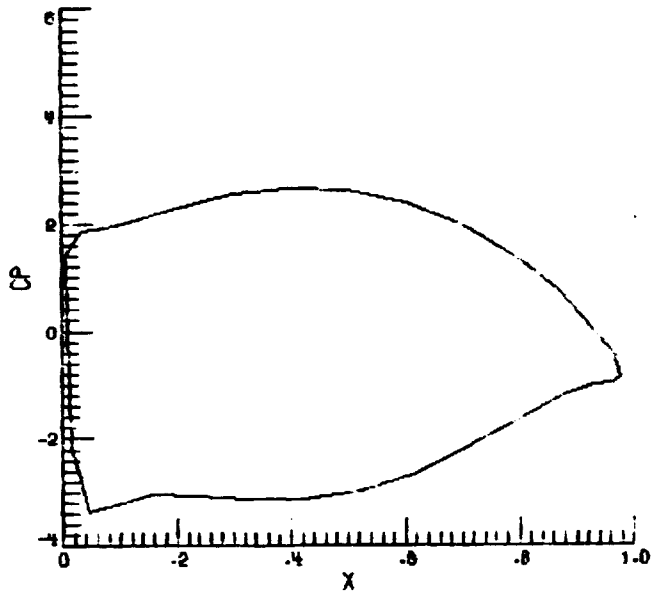


Figure 29. Pressure Distribution (NACA 0012) - $R_e$ = 1000, A = 12° t = 2.1, k = 4 (midspan)

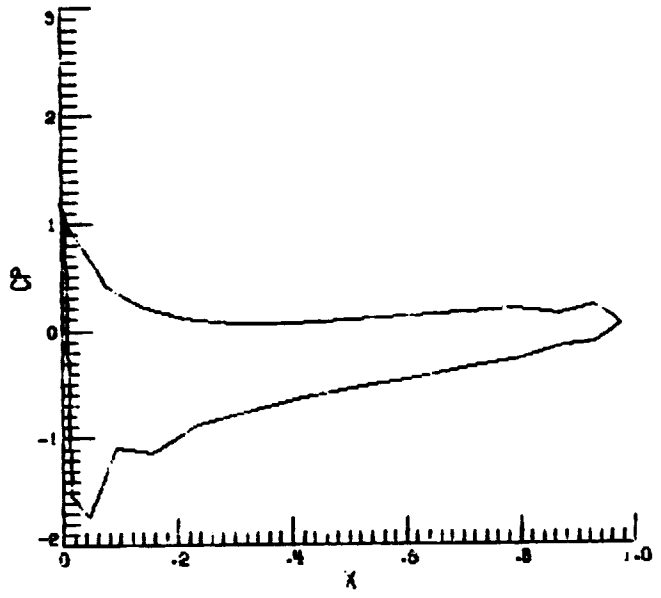


Figure 30. Pressure Distribution (NACA 0012) - $R_e$ = 1000, A = 12°, t = 2.5 , k = 4 (midspan)

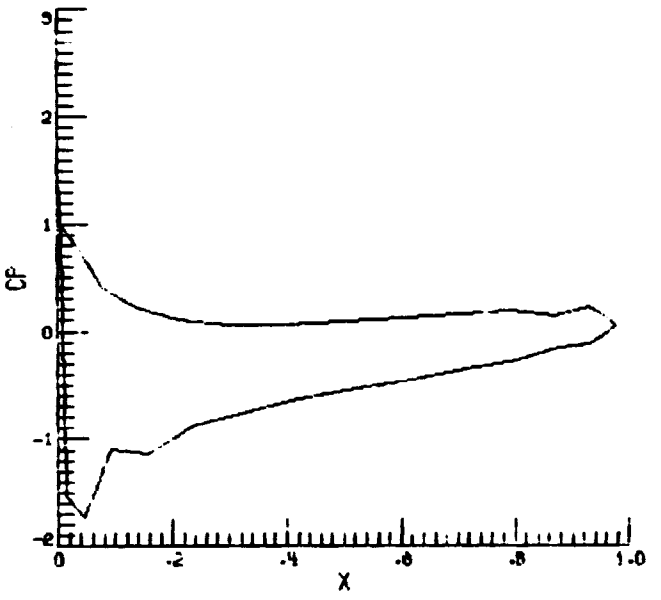


Figure 31. Pressure Distribution (NACA 0012) - $R_e$ = 1000, A = 12°, t = 2.6, k = 4 (midspan)

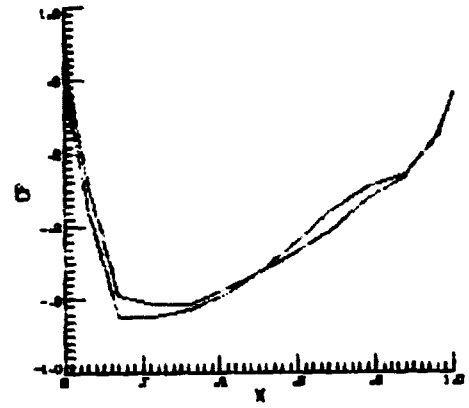

Figure 32. Pressure Distribution (NACA 663018) $R_e$ = 10,000, A = 0° t = 2.1, k = 4

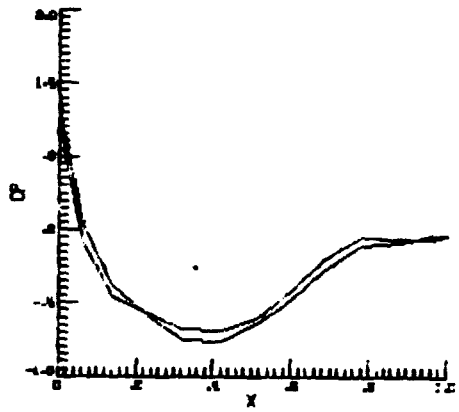

Figure 33. Pressure Distribution (NACA $66_3$018) $R_e$ = 10,000, A = 0° t = 2.2, k = 4

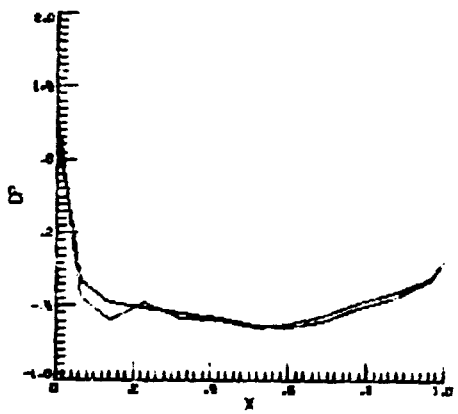

Figure 34. Pressure Distribution (NACA $66_3$018) - $R_e$ = 10,000, A = 0° t = 2.3, k = 4

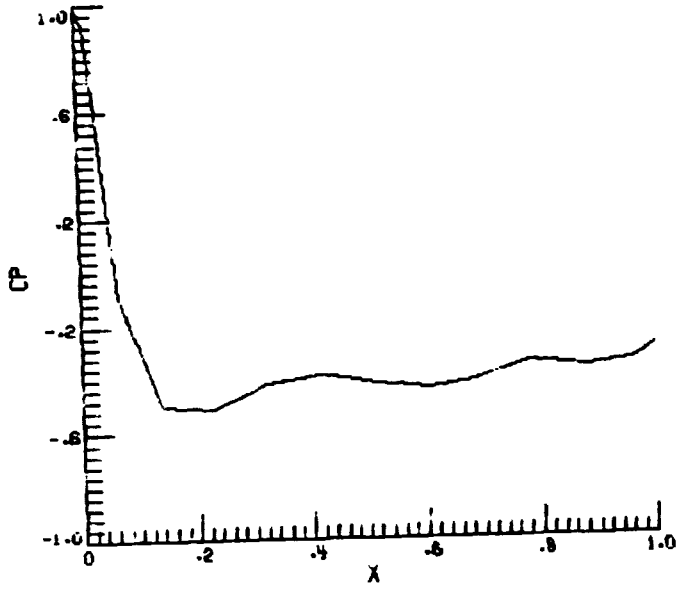


Figure 35. Pressure Distribution (NACA $66_3018$)
$R_e$ = 10,000, A = 0°, t = 2.9, k = 1 (wall)

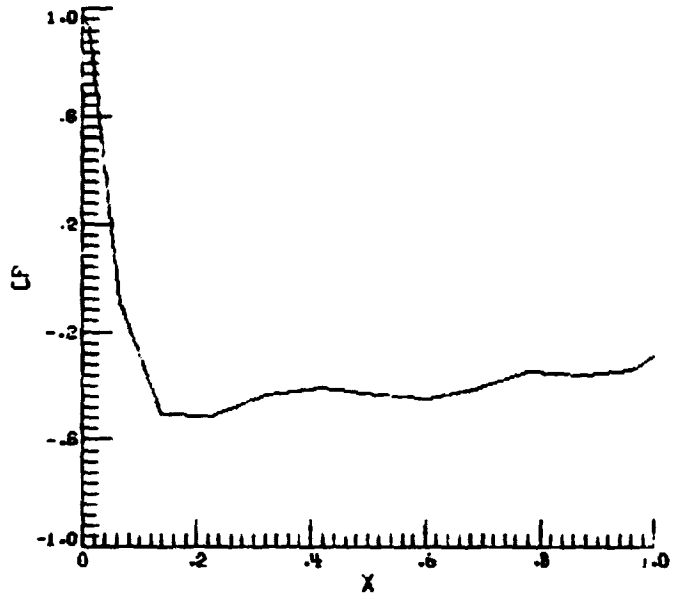


Figure 36. Pressure Distribution (NACA $66_3018$) - $R_e$ = 10,000, A = 0°, t = 2.9, k = 2

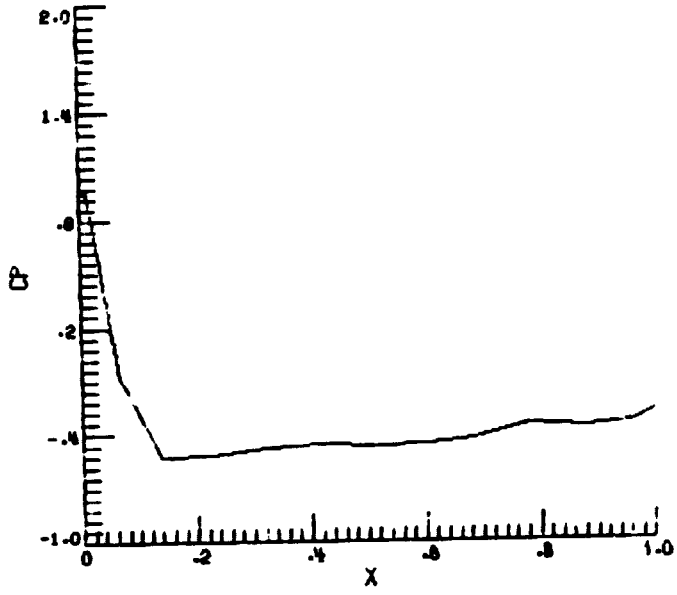


Figure 37. Pressure Distribution (NACA $66_3018$) - $R_e$ = 10,000, A = 0°, t = 2.9, k = 3

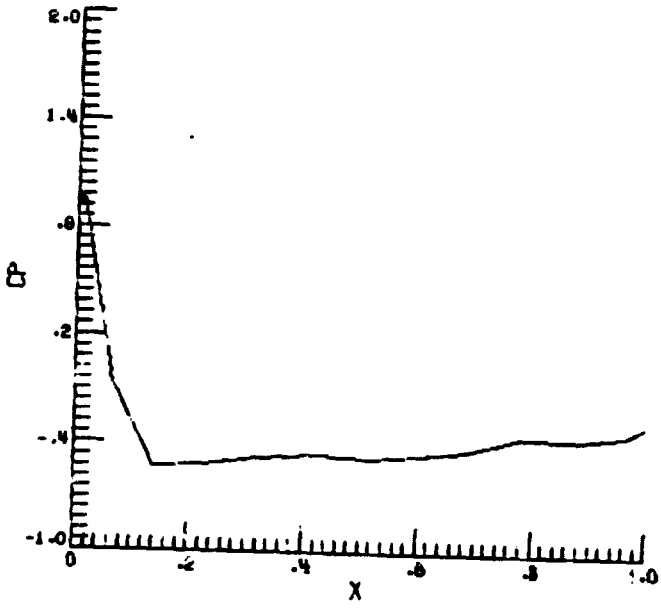


Figure 38. Pressure Distribution (NACA $66_3018$) - $R_e$ = 10,000, A = 0°, t = 2.9, k = 4 (midspan)

ORIGINAL PAGE IS
OF POOR QUALITY

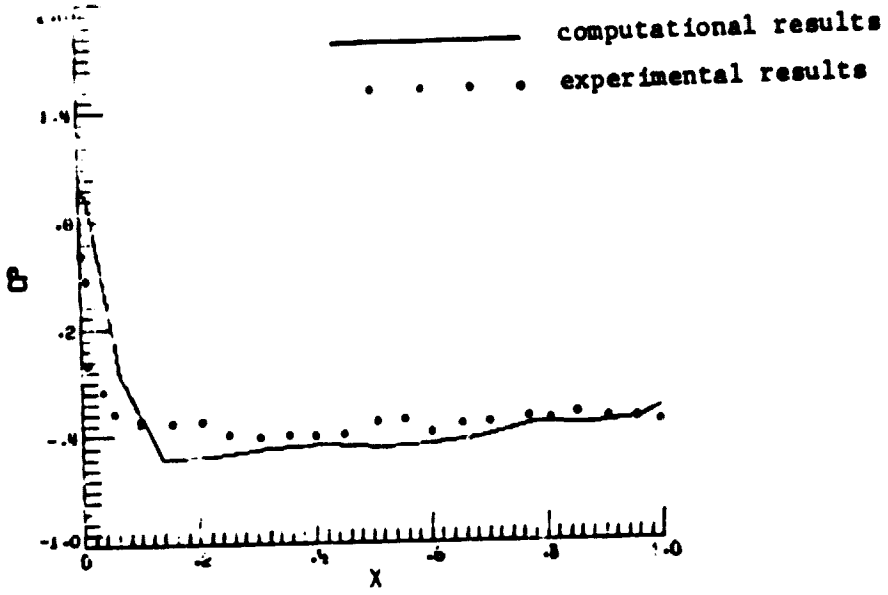


Figure 39. Comparison of Computational Results (NACA $66_3018$) at $R_e$ = 10,000 with Experimental Results at $R_e$ = 40,000, A = 0°

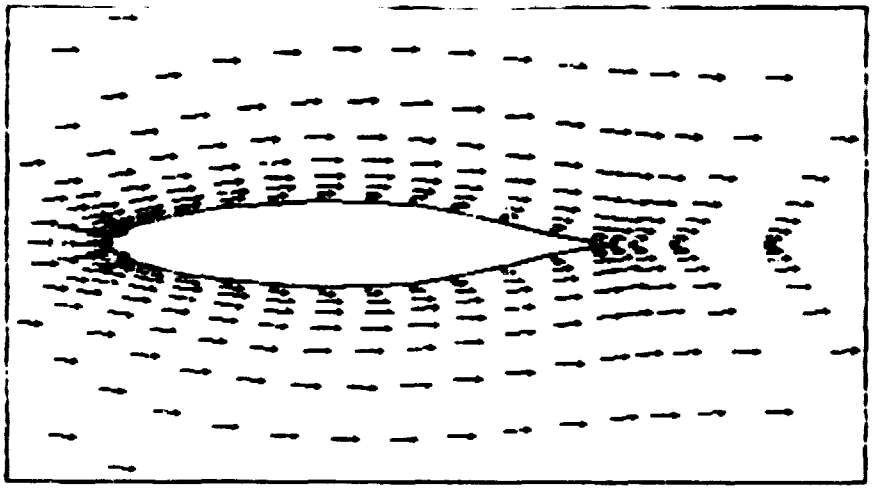

Figure 40. Velocity Profiles (NACA $66_3018$) - $R_e$ = 10,000, A = 0°, t = 2.9, k = 4 (midspan)

## APPENDIX A

### Relations and definitions in the transformed plane.

Contained herein are the pertinent relationships defining the transformations of the spatial derivatives, appearing in the governing equations, from the physical to the computational space. All the transformations are given in their fully non-conservative forms. The following notations for scalar and vector functions are valid throughout all the expressions.

$f(x,y,z,t)$ - A scalar funciton with at least two continuous derivatives.

$F(x,y,z) = \underset{\sim}{i}F_1(x,y,z) + \underset{\sim}{j}F_2(x,y,z) + \underset{\sim}{k}(x,y,z)$ - A continuously differentiable vector-valued function. $\underset{\sim}{i}$, $\underset{\sim}{j}$, and $\underset{\sim}{k}$ denote the Cartesian unit vectors.

Definitions of the transformations in 2-D grid generation.

$$\alpha_c = x_\eta^2 + y_\eta^2 \tag{A.1}$$

$$\psi_c = x_\xi x_\eta + y_\xi y_\eta \tag{A.2}$$

$$\gamma_c = x_\xi^2 + y_\xi^2 \tag{A.3}$$

$$J_c = x_\xi y_\eta - x_\eta y_\xi \tag{A.4}$$

Transformations in the three-dimensional space.

$$z = F(\zeta) \tag{A.5}$$

$$\alpha = \alpha_c F'^2(\zeta) \tag{A.6}$$

$$\beta = \gamma_c F'^2(\zeta) \tag{A.7}$$

$$\gamma = J_c^2 \tag{A.8}$$

$$\delta = -2(x_\xi x_\eta + y_\xi y_\eta)F'^2(\zeta) \tag{A.9}$$

$$\sigma = \frac{F'(\zeta)}{J}(x_\eta Dy - y_\eta Dx) \tag{A.10}$$

$$\tau = \frac{F'(\zeta)}{J}(y_\xi Dx - x_\xi Dy) \tag{A.11}$$

$$\phi = \frac{F''(\zeta)}{J}(x_\xi y_\eta - x_\eta y_\xi) \tag{A.12}$$

$$J = z_\zeta(x_\xi y_\eta - y_\xi x_\eta) = F'(\zeta)\,c \tag{A.13}$$

$$Dx = \alpha x_{\xi\xi} + \beta x_{\eta\eta} + \delta x_{\eta\xi} \tag{A.14}$$

$$Dy = \alpha y_{\xi\xi} + \beta y_{\eta\eta} + \delta y_{\eta\xi} \tag{A.15}$$

Derivative transformations

$$f_x = (\partial f/\partial x)_{y,z,t} = (y_\eta f_\xi - y_\xi f_\eta)/J_c \tag{A.16}$$

$$f_y = (\partial f/\partial y)_{x,z,t} = (x_\xi f_\eta - x_\eta f_\xi)/J_c \tag{A.17}$$

$$f_z = (\partial f/\partial z)_{x,y,t} = f(\zeta)/F'(\zeta) \tag{A.18}$$

$$\begin{aligned} f_{xx} = (\partial^2 f/\partial x^2)_{y,z,t} &= (y_\eta^2 f_{\xi\xi} - 2y_\xi y_\eta f_{\xi\eta} + y_\xi^2 f_{\eta\eta})/J_c^2 \\ &+ (y_\eta^2 y_{\xi\xi} - 2y_\xi y_\eta y_{\xi\eta} + y_\xi^2 y_{\eta\eta})(x_\eta f_\xi - x_\xi f_\eta)J_c^3 \\ &+ (y_\eta^2 x_{\xi\xi} - 2y_\xi y_\eta x_{\xi\eta} + y_\xi^2 x_{\eta\eta})(y_\xi f_\eta - y_\eta f_\xi)/J_c^3 \end{aligned} \tag{A.19}$$

$$f_{yy} = (\partial^2 f/\partial y^2)_{x,z,t} = (x_\eta^2 f_{\xi\xi} - 2x_\xi x_\eta f_{\xi\eta} + x_\xi^2 f_{\eta\eta})/J_c^2$$
$$+ (x_\eta^2 y_{\xi\xi} - 2x_\xi x_\eta y_{\xi\eta} + x_\xi^2 y_{\xi\eta})(x_\eta f_\xi - x_\xi f_\eta)J_c^3$$
$$+ (x_\eta^2 x_{\xi\xi} - 2x_\xi x_\eta x_{\xi\eta} + x_\xi^2 x_{\eta\eta})(y_\xi f_\eta - y_\eta f_\xi)/J_c^3 \quad (A.20)$$

$$f_{zz} = (\partial^2 f/\partial z^2)_{x,y,t} = [f_{\zeta\zeta} - f_\zeta F''(\zeta)/F'(\zeta)]/F'^2(\zeta) \quad (A.21)$$

$$f_{xy} = [x_\xi y_\eta + x_\eta y_\xi) f_{\xi\eta} - x_\xi y_\xi f_{\eta\eta} - x_\xi y_\xi f_{\eta\eta}]/J_c^2$$
$$+ [x_\eta y_\eta x_{\xi\xi} - (x_\xi y_\eta + x_\eta y_\xi)x_{\xi\eta} + x_\xi y_\xi x_{\eta\eta}](y_\eta f_\xi - y_\xi f_\eta)J_c^3$$
$$+ [x_\eta y_\eta y_{\xi\xi} - (x_\xi y_\eta + x_\eta y_\xi)y_{\xi\eta} + x_\xi y_\xi y_{\eta\eta}]$$
$$(x_\xi f_\eta - x_\eta f_\xi)/J_c^3 \quad (A.22)$$

$$f_{yz} = (f_{\eta\zeta} x_\xi - f_{\xi\xi} x_\eta)/J \quad (A.23)$$

$$f_{xz} = (f_{\xi\xi} y_\eta - f_{\eta\zeta} y_\xi)/J \quad (A.24)$$

The Laplacian Operator.

$$\nabla^2 f = (\alpha f_{\xi\xi} + \beta f_{\eta\eta} + \gamma f_{\zeta\zeta} + \delta f_{\xi\eta} + \sigma f_\xi + \tau f_\eta$$
$$+ \phi f_\zeta)/J^2 \quad (A.25)$$

Unit Normal Vectors.

Normal to $\eta$-surface:

$$\underset{\sim}{n}^{(\eta)} \equiv \nabla\eta/|\nabla\eta| = (-i y_\xi + j x_\xi)/\sqrt{\gamma_c} \quad (A.26)$$

Normal to $\xi$-surface:

$$\underset{\sim}{n}^{(\xi)} \equiv \nabla\xi/|\nabla\xi| = (i y_\eta - j x_\eta)/\sqrt{\alpha_c} \quad (A.27)$$

Directional Derivatives.

$$\partial f/\partial \underset{\sim}{n}^{(\eta)} \equiv \underset{\sim}{n}^{(\eta)} \cdot \underset{\sim}{\nabla} f = (\gamma_c f_\eta - \beta_c f_\xi)/J_c\sqrt{\gamma_c} \qquad \text{(A.28)}$$

$$\partial f/\partial \underset{\sim}{n}^{(\xi)} \equiv \underset{\sim}{n}^{(\xi)} \cdot \underset{\sim}{\nabla} f = (\alpha_c f_\xi - \beta_c f_\eta)/J_c\sqrt{\gamma_c} \qquad \text{(A.29)}$$

$$\partial f/\partial \underset{\sim}{n}^{(\zeta)} \equiv \underset{\sim}{n}^{(\zeta)} \cdot \underset{\sim}{\nabla} f = f_\zeta/F'(\zeta) \qquad \text{(A.30)}$$

## APPENDIX B

### Optimum acceleration parameters.

The Navier-Stokes equations in non-conservative primitive variable formulation fit the description of the following general partial differential equation in the transformed plane.

$$A_1 f_{\xi\xi} + A_2 f_{\eta\eta} + A_3 f_{\zeta\zeta} + B_1 f_{\xi} + B_2 f_{\eta} + B_3 f_{\zeta} + Cf + D = 0 \quad \text{(B.1)}$$

f identifies itself with u, v or w in the x, y or z-momentum equation.

The spectral radius $\rho_j$ for Jacobi iteraion of a set of IMAX x JMAX x KMAX simulataneous difference equations with constant coefficients [14] is given by,

$$\rho_j = \frac{1}{|C - 2(A_1 + A_2 + A_3)|} \left[ \sqrt{|4A_1^2 - B_1^2|}\, \cos\left(\frac{\pi}{IMAX + 1}\right) + \sqrt{|4A_2^2 - B_2^2|}\, \cos\left(\frac{\pi}{JMAX + 1}\right) + \sqrt{|4A_3^2 - B_3^2|}\, \cos\left(\frac{\pi}{KMAX + 1}\right) \right] \quad \text{(B.2)}$$

The optimum acceleration parameters w, for SOR iteration are easily obtained utilizing $\rho_j$ in the following expression,

$$\omega = \frac{2}{1 + \sqrt{1 - \rho_j^2}} \quad \text{if } 4A_1^2 \geq B_1^2,\ 4A_2^2 \geq B_2^2 \text{ and } 4A_3^2 \geq B_3^2 \quad \text{(B.3)}$$

and,

$$\omega = \frac{2}{1 + \sqrt{1 + \rho_j^2}} \quad \text{otherwise.} \quad \text{(B.4)}$$

The coefficients in equations (B.1) are listed on the following page.

Coefficients in the x-momentum equation:

$$A_1 = R_1 \tag{B.5}$$

$$A_2 = R_2 \tag{B.6}$$

$$A_3 = R_3 \tag{B.7}$$

$$B_1 = T_1 + \frac{1}{R_e J_c}\left(2\mu_x y_\eta - \mu_y x_\eta\right) \tag{B.8}$$

$$B_2 = T_2 + \frac{1}{R_e J_c}\left(-2\mu_x y_\xi + \mu_y x_\xi\right) \tag{B.9}$$

$$B_3 = T_3 + \frac{\mu_z}{R_e}\,\frac{1}{F'(\zeta)} \tag{B.10}$$

$$C = -\frac{T}{\Delta t} \tag{B.11}$$

Coefficients in the y-momentum equation:

$$A_1 = R_1 \tag{B.12}$$

$$A_2 = R_2 \tag{B.13}$$

$$A_3 = R_3 \tag{B.14}$$

$$B_1 = T_1 + \frac{1}{R_e J_c}\left(-2\mu_y x_\eta + \mu_x y_\eta\right) \tag{B.15}$$

$$B_2 = T_2 + \frac{1}{R_e J_c}\left(2\mu_y x_\xi - \mu_x y_\xi\right) \tag{B.16}$$

$$B_3 = T_3 + \frac{\mu_z}{R_e}\,\frac{1}{F'(\zeta)} \tag{B.17}$$

$$C = -\frac{T}{\Delta t} \tag{B.18}$$

Coefficients in the z-momentum equation:

$$A_1 = R_1 \tag{B.19}$$

$$A_2 = R_2 \tag{B.20}$$

$$A_3 = R_3 \tag{B.21}$$

$$B_1 = T_1 + \frac{1}{R_e J_c}\left(\mu_x y_\eta - \mu_y x_\eta\right) \tag{B.22}$$

$$B_2 = T_2 + \frac{1}{R_e J_c}\left(-\mu_x y_\xi + \mu_y x_\xi\right) \tag{B.23}$$

$$B_3 = T_3 + \frac{2\mu_z}{R_e}\,\frac{1}{F'(\zeta)} \tag{B.24}$$

$$C = -\frac{T}{\Delta t} \tag{B.25}$$

The repeated terms in the above expressions are:

$$R_1 = \frac{\mu}{R_e J^2}\,\alpha \tag{B.26}$$

$$R_2 = \frac{\mu}{R_e J^2}\,\beta \tag{B.27}$$

$$R_3 = \frac{\mu}{R_e J^2}\,\gamma \tag{B.28}$$

$$T_1 = \frac{1}{J_c}\left(-uy_\eta - vx_\eta\right) + \frac{\mu}{R_e J^2}\,\sigma \tag{B.29}$$

$$T_2 = \frac{1}{J_c}\left(uy_\xi - vx_\xi\right) + \frac{\mu}{R_e J^2}\,\tau \tag{B.30}$$

$$T_3 = \frac{w}{F'(\zeta)} + \frac{\mu}{R_e J^2}\,\phi \tag{B.31}$$

$T = 1$ for first-order time differencing (B.32)

$T = \frac{3}{2}$ for second-order time differencing (B.33)

## BIBLIOGRAPHY


1. Graves, Randolph A., "Computational Fluid Dynamics, the Coming Revolution," Aeronautics and Astronautics, Vol. 20, (1982).

2. Thompson, Joe F., Thames, Frank C., and Mastin, C. Wayne, "Boundary-Fitted Curvilinear Coordinate Systems for Solution of Partial Differential Equations on Fields Containing Any Number of Arbitrary Two-Dimensional Bodies," NASA CR-2729.

3. Sorenson, Reese L., "A Computer Program to Generate Two-Dimensional Grids About Airfoils and Other Shapes by the Use of Poisson's Equation," NASA Technical Memorandum 81198.

4. Beam, R. M., and Warming, R. F., "An Implicit Factored Scheme for the Compressible Navier-Stokes Equations," AIAA Paper 77-645, AIAA 3rd Computational Fluid Dynamics Conference (1977).

5. Steger, Joseph L., and Kutler Paul, "Implicit Finite-Difference Procedures for the Computation of Vortex Wakes," AIAA Journal, Vol. 15, (1977).

6. Bernard, Robert S., and Thompson, Joe F., "Approximate Factorization with an Elliptic Pressure Solver for Incompressible Flow," AIAA Paper 82-0978, AIAA/ASME 3rd Joint Thermophysics, Fluids, Plasma and Heat Transfer Conference, (1982).

7. East, J. L. and Pierce, F. J., "Explicit Numerical Solution of the Three-Dimensional Incompressible Turbulent Boundary-Layer Equations," AIAA Journal, Vol. 10, (1972).

8. Thompson, Joe F., et. al., "Automatic Numerical Generation of Body-Fitted Curvilinear Coordinate System for Field Containing Any Number of Arbitrary Two-Dimensional Bodies," Journal of Computational Physics, Vol. 15, (1974).

9. Baldwin, B. S., and Lomax, H., "Thin Layer Approximation and Algebraic Model for Separated Turbulent Flows," AIAA Paper 78-257, AIAA 16th Aerospace Sciences Meeting, (1978).

10. Thompson, Joe F., and Mastin, C. W., "Grid Generation Using Differential Systems Techniques," Numerical Grid Generation Techniques, NASA Conference Publication 2166, (1980).

11. Hodge, J. K., "Numerical Solution of Incompressible Laminar Flow About Arbitrary Bodies in Body-Fitted Curvilinear Coordinate," Ph.D. Dissertation, Mississippi State University, (1975).

12. Shanks, S. P., "Numerical Simulation of Viscous Flow About Submerged Arbitrary Hydrofoils Using Non-Orthogonal, Curvilinear Coordinate," Ph.D. Dissertation, Mississippi State University, (1977).

13. Thompson, David S., "Numerical Solution of the Navier-Stokes Equations for High Reynolds Number Incompressible Turbulent Flow," M.S. Thesis, Mississippi State University, (1980).

14. Thompson, J. F., Personal Communication, Department of Aerospace Engineering, Mississippi State University, Mississippi State, Mississippi (1981).

15. Mueller, T. J., Jansen, B. J., Bernard, R. S., and Thompson, J. F., "Computers in Flow Predictions and Fluid Dynamics Experiments," The Winter Annual Meeting of the American Society of Mechanical Engineers, ASME Publication (1981).